Received: 6 March 2024 | Revised: 24 June 2024 | Accepted: 1 July 2024

DOI: 10.1002/hyp.15240

RESEARCH ARTICLE

WILEY

Physical and chemical characterization of remote coastal aquifers and submarine groundwater discharge from a glacierized watershed

A. A. Russo[1,2] | J. Jenckes[3] | D. F. Boutt[4] | J. Munk[5] | A. Kirshen[4] | L. A. Munk[1]

[1]Department of Geological Sciences, University of Alaska Anchorage, Anchorage, Alaska, USA

[2]Department of Geosciences, University of Alaska Fairbanks, Anchorage, Alaska, USA

[3]Department of Chemistry, University of Alaska Anchorage, Anchorage, Alaska, USA

[4]Department of Geosciences, University of Massachusetts Amherst, Amherst, Massachusetts, USA

[5]Department of Electrical Engineering, University of Alaska Anchorage, Anchorage, Alaska, USA

Correspondence
Russo A. A., Department of Geological Sciences, University of Alaska Anchorage, Anchorage, Alaska, USA.
Email: arusso3@alaska.edu

Abstract

Coastal aquifers play an important role in marine ecosystems by providing high fluxes of nutrients and solutes via submarine groundwater discharge pathways. The physical and chemical characterization of these dynamic systems is foundational to understanding the extent and magnitude of hydrogeologic processes and their subsequent contributions to the marine environment. We describe a km-scale experimental field site located in a glaciofluvial delta entering Kachemak Bay, Alaska. Our characterization applies geophysical (ERT and HVSR), hydrogeologic (grain size analyses, slug tests and tidal response analyses) and geochemical (major ions and stable water isotopes) methods to describe the complexity of coastal aquifers in proglacial environments currently experiencing rapid transformations. The hydrogeologic and geophysical techniques revealed thick (20–84 m) sediments dominated by sands and gravels and delineated zones of freshwater, brackish water and saltwater at both high and low tides within the subterranean estuary. Estimates of hydraulic conductivities via multiple approaches ranged from 2 to 250 m d^{-1}, with means across the four methods within the same order of magnitude. Tidal response analyses highlighted a coastal aquifer in strong connection with the sea as evidenced by clear spring- and neap-tidal signals within a proximal piezometric hydrograph. Geochemical sampling revealed coastal groundwaters as substantially enriched in solutes compared to proximal river samples with limited variability across seasons. A clear connection between the Wosnesenski River and the adjacent aquifer was also observed, with concentrated recharge from the river corridor during the meltwater season. This combination of approaches provides the basis for a conceptual model for coastal aquifer systems within the Gulf of Alaska and an upscaled mean daily yield of freshwater and solutes

from the delta subsurface. Our findings are critical for subsequent numerical simulations of groundwater flow, tidal pumping and chemical reactions and transport in these understudied environments. This approach may be applied for low-cost, large-scale hydrogeologic investigations in coastal areas and may be particularly useful for remote sites where access and mobility are challenging.

KEYWORDS
coastal aquifer, coastal hydrogeology, conceptual model, geochemistry, geophysics, submarine groundwater discharge

1 | INTRODUCTION

Following the oceans and the cryosphere, groundwater is the third largest reservoir of the global hydrosphere and is by far the largest reserve of liquid freshwater (Shiklomanov & Rodda, 2003). Groundwater is estimated to provide 36% of the drinking water supply globally, and is an optimal source of freshwater because it supports withdrawals during dry periods and is often of higher quality than surface waters (Burke & Moench, 2000; Döll et al., 2012). Coastal aquifer systems are especially valuable as one of the primary contributors of freshwater, solutes and nutrients from land to sea (Taniguchi et al., 2019). A dynamic relationship between a dense wedge of saline water propagating from coastal processes merging with fresh, gradient-driven groundwaters of the terrestrial domain lies unseen beneath the surface. This interface is termed the subterranean estuary (STE) and has been recognized as a vastly important biogeochemical hotspot for the cycling of elements that have a substantial influence on near-shore ecosystems (Johannesson et al., 2017; Knee & Paytan, 2011; Moore, 1999; Santos et al., 2021; Slomp & Van Cappellen, 2004). Water eventually exits the STE as submarine groundwater discharge (SGD), which is the flow of water from porous media to the ocean, regardless of whether it originates as recirculated seawater or as fresh, terrestrial groundwater (fresh SGD; Burnett et al., 2003). The current knowledge of this important resource is limited compared to surface water resources, especially in data-scarce and widely inaccessible regions.

One of the greatest hydrological regime shifts ever experienced on Earth is underway in the Gulf of Alaska (GoA). Glaciers along the GoA coastline are losing mass more rapidly than any other glacierized region (Zemp et al., 2019), although peak water is predicted to occur the latest of all regions globally (Huss & Hock, 2018). The glacier mass loss from this basin alone accounts for 7% of global sea level rise, or 0.211 ± 0.016 mm year^{-1} (Huss & Hock, 2018; Jakob et al., 2021). Additionally, precipitation changes due to warming air temperatures are increasing rainfall while diminishing snowpacks (Bieniek et al., 2014; Shanley et al., 2015). These climate-driven mediations have spawned an extensive research focus on the hydrology of the GoA basin. Rapid transformations are occurring in the seasonality and mass of freshwater (Beamer et al., 2017; Mizukami et al., 2022; Young et al., 2021), nutrients and solutes (Bergstrom et al., 2021; Fellman et al., 2015; Hood et al., 2020; Hood & Berner, 2009; Hood & Scott, 2008; Jenckes et al., 2022), trace metals (Crusius et al., 2011; Hawkings et al., 2018; Raiswell et al., 2006; Schroth et al., 2011) and sediment (Anderson, 2005; Hallet et al., 1996; Jenckes et al., 2023) that are delivered to coastal environments. This is effectuating extensive modifications on oceanographic properties (Hauri et al., 2020; Johnson, 2021) and near-shore ecosystems (Hood & Berner, 2009; O'Neel et al., 2015; Weitzman et al., 2021; Whitney et al., 2018). One major component of the hydrology of the GoA has received insufficient attention. Coastal groundwater is a meaningful source from which freshwater, trace metals, nutrients and solutes are delivered to coastal environments (Moore, 2010) and aquifers along the GoA margin are likely to experience significant alterations in the dramatic hydroclimatic shift that is occurring (Russo et al., 2023).

Responsible coastal water management within the GoA has considerable consequences on the thriving fisheries, aquaculture, tourism, subsistence communities and culture therein. SGD is an integral part of the effective management of coastal waters, and there is a need for a comprehensive understanding of the groundwater systems within this vast coastline. SGD often provides more nutrients than proximal surface water sources (Kim et al., 2005; Rodellas et al., 2015; Swarzenski et al., 2007; Taniguchi et al., 2019), and contributes significantly to the flux of trace metals and rare earth elements (Johannesson et al., 2017; Szymczycha et al., 2016). Recent investigations in the Arctic revealed dissolved chemical fluxes that are up to two orders of magnitude higher than rivers (Connolly et al., 2020) and identified unique circulation mechanisms (Guimond et al., 2023). Across the globe, SGD has been observed to express a dominant influence over fisheries (Lilkendey et al., 2019; Peng et al., 2021; Spalt et al., 2020), near-shore environments and biological structures (Johannesson et al., 2017; Lecher & Mackey, 2018; Moore, 1996, 2010; Santos et al., 2021), as well as meeting requirements for functioning human societies (Alorda-Kleinglass et al., 2021; Moosdorf & Oehler, 2017). In the GoA, a recent study estimated SGD as a primary nitrate and silicic acid source to a semi-enclosed bay with economic mariculture activity (Haag et al., 2023). These pathways can also serve as an effective conduit for pollutants to reach coastal areas (Lecher et al., 2015) and be a catalyst for eutrophication and the initiation of red tides (Kurtz et al., 2023; Luo & Jiao, 2016).

Climate-mediated changes are expected to impact groundwater resources negatively (Kundzewicz & Doell, 2009; Michael et al., 2013; Richardson et al., 2024), particularly at high latitudes (Guimond et al., 2022) and in mountain environments (Somers & McKenzie, 2020). Extreme rainfall events have been observed to induce high

SGD rates and increase nutrient delivery to coastal waters (Diego-Feliu et al., 2022). Degradation of the cryosphere coincides with radical land cover changes (Lane et al., 2017), which may significantly alter groundwater recharge zones and storage (Bouraoui et al., 1999; Mackay et al., 2020). Additionally, rapid uplift from negative ice mass balance will increase topographic gradients to the coast (Larsen et al., 2004), increasing fresh SGD in turn. Advancing our knowledge of the current conditions of these systems will enable intelligent counteractions to the effects of a rapidly changing landscape.

Whereas rivers and estuaries are easy to sample and monitor at discrete locations, there are obvious difficulties in obtaining measurements from the unseen groundwater component of the water cycle. A suite of multidisciplinary methods has been established in recent decades to assess the contribution of SGD to the marine system. Various approaches may be grouped into three general categories: modelling, direct physical measurements and geochemical tracer techniques. Modelling techniques range from simple water balance calculations (Hajati et al., 2019; Prakash et al., 2018; Russo et al., 2023; Zhou et al., 2019) to complex, dual-density numerical models (Michael, 2005; Michael et al., 2016; Paldor et al., 2022; Robinson, Gibbes, et al., 2007; Robinson, Li, & Barry, 2007). Direct point measurements of the SGD flux are commonly measured using manual or automated seepage metres (Michael et al., 2003; Sholkovitz et al., 2003; Taniguchi et al., 2003). Methods using piezometers in a transect exploit measurements of the gradient of hydraulic head combined with the application of Darcy's law (Kroeger et al., 2007; Mulligan & Charette, 2006). Geochemical approaches that use natural tracers to quantify SGD at local and regional scales have seen widespread application in recent decades (Burnett et al., 2007; Kwon et al., 2014; Rocha et al., 2016). Geophysical approaches have also been applied to map out variations in temperature and salinity within coastal aquifers, although they must be combined with other methods to quantify the SGD flux (Taniguchi et al., 2019). These include the detection of groundwater plumes via thermal infrared sensing of sea surface temperatures (Lee et al., 2016; Varma et al., 2010), delineation of saltwater and freshwater domains via electrical resistivity (Dimova et al., 2012; Stieglitz et al., 2008; Taniguchi et al., 2008), and identification of subsurface features and morphology via seismic profiling (Mulligan et al., 2007; Stieglitz, 2005; Viso et al., 2010).

In this study we provide an efficient and economical means to develop a preliminary characterization of coastal aquifer systems, which may be particularly useful in remote and difficult to access locations. We combine site instrumentation for long-term monitoring of groundwater levels and geochemical sampling across seasons with a combination of geophysical and hydraulic approaches. The geophysical methods allow us to delineate aquifer domains and salinity profiles, which subsequent hydraulic methods require to estimate physical aquifer parameters, such as hydraulic conductivity. Darcy flux calculations and solute yields are presented by aggregating the hydraulic characterization and geochemical monitoring. Long-term geochemical monitoring of groundwater and proximal streams also allows for directly comparing these waters' contributions to the marine system. Furthermore, the components of this characterization are fundamental for subsequent numerical flow and reactive transport simulations of SGD to the GoA. An evident lack of effort is applied to quantify SGD and associated solute deliveries at the local scale in high-latitude mountain regions. This multidisciplinary investigation is a major step in determining these groundwater systems' current conditions and fate along the GoA margin.

2 | STUDY AREA

2.1 | Wosnesenski River Delta experimental site, Kachemak Bay, Alaska

2.1.1 | Geologic, hydrogeologic and oceanographic context

The Wosnesenski River is a proglacial stream draining the western flanks of the Grewingk-Yalik Ice Complex in the southern Kenai Mountains of south-central Alaska. The bedrock geology of the Wosnesenski River watershed is entirely composed of the McHugh Complex, which is part of a Mesozoic accretionary prism known as the Chugach terrane that developed from off scraping and/or underplating at an ancient subduction zone (Bradley et al., 1992). Rock types of the McHugh Complex include variably distributed greenstone, chert, argillite, graywacke, conglomerate, outcrop-scale mélange and rare limestone that have been intruded by a variety of igneous rocks (Clark et al., 1973). The current geologic setting of the Kenai Mountains is within the arc-trench gap of the Aleutian subduction system. Deformation at the surface has resulted in primarily east-northeast striking late brittle faults that occur in abundance throughout the mountain range with widespread, sub-horizontal shortening in the NW-SE direction (Kusky & Bradley, 1999). Glaciers have periodically dominated the landscape throughout the Quaternary period, with surficial deposits indicating that at least five major glacial periods occurred within the region during the Pleistocene (Schmoll & Yehle, 1986). The current ice surface is at an elevation of around 1200 m, with peaks protruding out to elevations up to 2000 m (Wiles & Calkin, 1994). Equilibrium line altitudes in the area have risen on the order of 500 m between the Late Wisconsin maximum and the present (Wiles, 1992). Glaciers of the Grewingk-Yalik Ice Complex are all currently retreating rapidly, with comparative satellite imagery revealing average retreat rates of 45 m $year^{-1}$ between 1950 and 2005.

The Wosnesenski River empties from the Kenai Mountains into Kachemak Bay, creating a tide-dominated fan-delta. The Wosnesenski River and its delta have a total area of 267 km^2, 26% of which is currently covered by glaciers. The Wosnesenski River Delta (WRD), the focus of our characterization, extends along 13 km of the Kachemak Bay coastline. The WRD is solely accessible by landing craft, as no roads connect to this remote, isolated location. Kachemak Bay is the largest estuarine reserve in the National Estuarine Research Reserve System. It is also one of the most diverse and productive estuaries in Alaska, with an abundance of whales, porpoises, Stellar sea lions, seals, sea otters, five species of Pacific salmon, halibut, herring, tanner crabs, Dungeness crabs, king crabs, several species of clams and oysters and other fauna (NERR website). The recent retreat of glaciers

lining the southern shore of the bay has resulted in habitat degradation (Traiger & Konar, 2017). Studies that connect marine communities to coastal groundwater systems are not currently part of the research scope in the GoA.

The surface of the WRD is dominated by a heterogeneous mix of coarse glaciogenic sand and gravel, with lesser occurrences of silt in the subaerial domain. Thick layers of this predominately coarse material enable abundant phreatic storage within the delta and an extensive mixing zone for biogeochemical reactions. The morphology of the WRD is dictated by (1) the supply of glaciogenic sediments distributed by the Wosnesenski River and its proximal valley glaciers as it changes course laterally, (2) modifications from the high-energy marine environment and (3) tectonic activity. In recent geologic history, the 1964 Valdez earthquake redirected the mouth of the river nearly 2.5 km south of its previous position, coinciding with 1–2 m of subsidence in the area (Coulter & Migliaccio, 1966). In Homer, directly across Kachemak Bay from the WRD (~5 km), the mean maximum semidiurnal tidal range is 5.6 m, with extreme tides exceeding 9 m. Mean wave heights are 0.5 and 0.8 m for summer and winter, respectively, although they have been observed in excess of 2.5 m (Adams et al., 2007). These oceanographic conditions enable a powerful means to recirculate seawater back through the porous media of the WRD and effectively pump nutrients and solutes via SGD pathways.

2.1.2 | Hydroclimate

The Aleutian low-pressure centre, which forces a counter-clockwise circulation over the GoA, dominates the climate of the Kenai Mountains (Daigle & Kaufman, 2009). This recruits a rather high mean annual precipitation of 1730 mm $year^{-1}$ to the town of Seward, Alaska on the eastern side of the range. The precipitation shadow effect greatly diminishes the supply of rain and snow to the western flanks, with Homer, Alaska receiving 635 mm annually. Homer has a mean air temperature of 3.3°C, which has increased rapidly over the past 70 years by 5.5°C and 2.3°C for mean summer and winter temperatures, respectively (Jenckes et al., 2023). Average annual snowfall within the Wosnesenski watershed from 1980 to 2023 is 865 cm $year^{-1}$ (extracted from Modern Era Retrospective Analysis for Research and Applications; Rienecker et al., 2011). The Wosnesenski River experiences three peaks in its discharge signal throughout the year: (1) from melting snowpack, typically in June, (2) from melting ice in proximal valley glaciers in July and August and (3) from the onset of the rainy season when peak precipitation occurs typically during September and October.

3 | METHODS

3.1 | Geophysical characterization

Geophysical studies offer an efficient and cost-effective means for an initial evaluation of the subsurface and are particularly valuable once integrated with other hydraulic and geochemical data. We implement several geophysical methods to provide preliminary and provisional data to support our hydrogeologic investigation of the WRD. The methods overviewed in this section allowed the geometry of the aquifer to be defined, provided aquifer thicknesses required for subsequent methods, and delineated zones of saltwater, brackish water and freshwater within the near-shore subsurface.

3.1.1 | Electrical resistivity tomography

Direct current electrical resistivity tomography (DC-ERT) was deployed to delineate the STE of the WRD. Data were acquired using an 84-electrode, Earth Resistivity/IP Meter Super Sting R1 IP (Advanced Gesoscienes Inc.). A dipole–dipole array was chosen over other commonly used arrays (e.g. Wenner, Schlumberger) due to its improved resolution, particularly in imaging lateral variations in resistivity cross-sections. Images were obtained using the RES2DINV software package (Loke & Barker, 1995), generating a two-dimensional resistivity cross-section that seeks to minimize the root-mean-square error between measured and simulated apparent resistivities. This software was also used to correct for differences in surface topography along a transect. Two DC-ERT surveys were conducted perpendicular to the shoreline during low and high tidal events on 7 July 2020 to compare the subsurface resistivity resulting from variations of the SW-FW interface over a semidiurnal tidal cycle. A difference plot was calculated by subtracting the resistivities at low tide from those at high tide to observe locations with significant variation between tides. An additional transect was conducted parallel with the shoreline during low tide to observe variability across the shoreface.

3.1.2 | Estimating depth to bedrock from horizontal-to-vertical spectral ratio seismic methods

Reliable sediment thickness and geometry estimations are key components of hydrogeologic investigations. We use a passive seismic technique that can be applied in remote locations to estimate the depth to bedrock rapidly. The horizontal-to-vertical spectral ratio (HVSR) approach records ambient noise from the Earth at a single, broadband, three-component seismometer that simultaneously records horizontal and vertical components of the seismic field at a given location (Ibs-von Seht & Wohlenberg, 1999; Molnar et al., 2018; Nakamura, 1989). The fundamental site resonance frequency is determined from the averaged ratio between the horizontal and vertical spectrum, which can then be applied to estimate sediment thickness using power-law regression equations (Haefner et al., 2010; Lane Jr et al., 2008; Panthi et al., 2023; Setiawan et al., 2018). We developed the first calibration curve for Southcentral Alaska by collecting HVSR readings at sites with known depth to bedrock. Sites of bedrock-penetrating water wells provided by the Alaska Department of Natural Resources Well Log Tracking System (WELTS) database were chosen to develop a local power-regression law equation necessary for surficial sediment thickness estimation (https://dnr.alaska.gov/welts/; last accessed 12 December 2023).

The primary seismic system we used to acquire HVSR data were the MoHo Tromino (MOHO Science and Technologies, Italy). Data were collected at each site for a minimum of 30 min and processed with the Grilla software package to remove anthropogenic noise, convert the time domain to the frequency domain, compute and plot the spectral ratio curve and determine the site's resonance frequency. Data acquisition and processing procedures followed user guidelines established under the SESAME project (Bard & Participants, 2004).

3.2 | Experimental site instrumentation

Three proximal onshore piezometers were installed in September 2021 and April 2022 to monitor and sample the shallow groundwater within the WRD (Figure 1). Solinst Model 615 stainless steel drive points with 3.175-cm steel pipe were driven manually between 1.4 and 3.8 m deep (Table 1). This approach is much more cost and time effective in remote, difficult to access locations than hiring a private drilling company. Piezometer locations were placed in a transect between the modern Wosnesenski River and Kachemak Bay along the banks of an abandoned channel. We used Solinst LTC loggers to continuously record water level, temperature and electrical conductivity of groundwater at 15-min intervals. Air temperature and barometric pressure were recorded to apply atmospheric corrections to sensor measurements. A river sensor that was originally deployed near the Pz1 site (Figure 1) was buried during melt-water floods in July 2022, with several unsuccessful recovery attempts made afterward.

3.3 | Hydraulic properties characterization: Multiple scales of inquiry

In this study, we apply several methods to quantify the hydraulic parameters of the WRD from local to aquifer scales. This

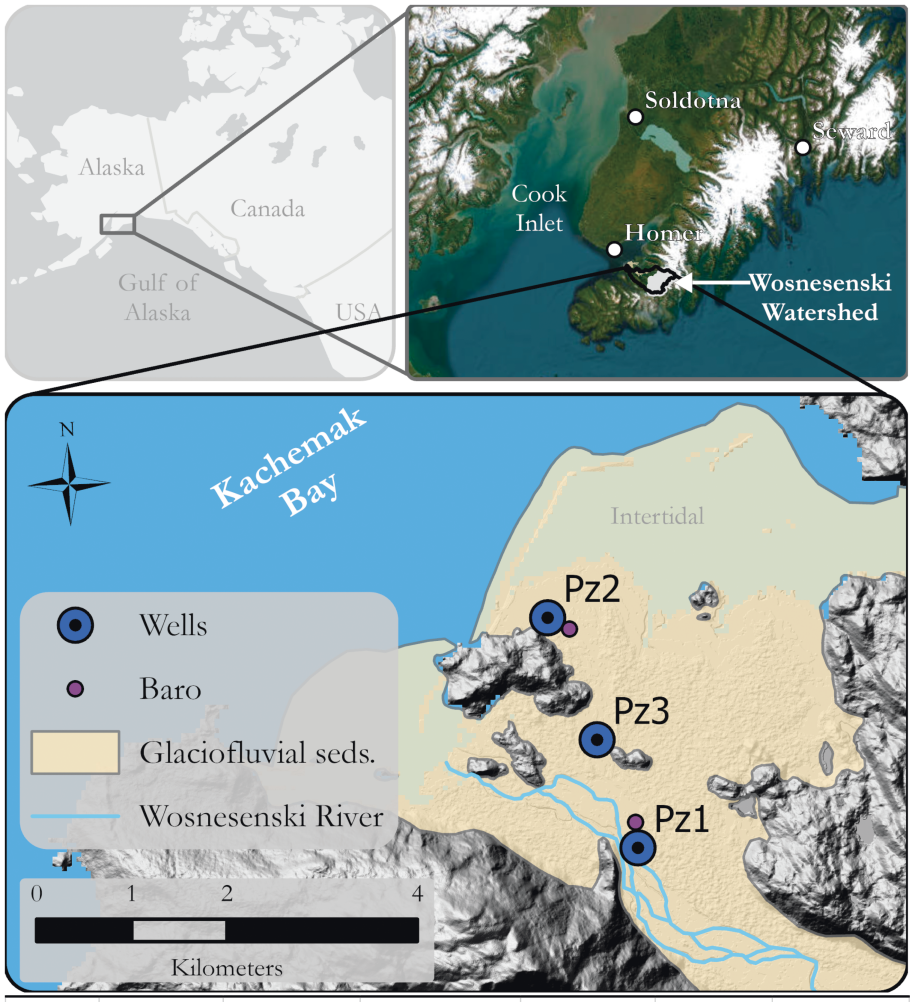

FIGURE 1 Experimental site location with insets provided in the top panel. The distribution of piezometers and barologgers are provided as blue and purple circles, respectively. Glaciofluvial sediments are depicted in beige, with lighter colours indicating intertidal zones. Undivided bedrock geology of the McHugh complex is drawn in shaded relief. Specifications of piezometers are described in tabular format below the main site map (PT, pressure transducer).

Site ID	Latitude (WGS 84)	Longitude (WGS 84)	Elevation land surface (masl)	Screen depth (cm)	Stickup (cm)	PT depth (cm)
Pz1	59.53205	-151.33965	15.0	193	44	144
Pz2	59.55399	-151.35475	5.6	383	21	360
Pz3	59.54235	-151.34645	10.4	362	40	233

TABLE 1 Mean hydraulic conductivity results from slug tests.

Site ID	*K* (m/d) KGS model	*K* (m/d) Horslev	*K* (m/d) Bouwer-Rice	Standard deviation (m/d)	K_{avg} (m/d)
Pz1	26	28	27	18	27
Pz2	1.8	2.8	2.6	0.5	2
Pz3	28	30	19	6	26

characterization includes measurements of hydraulic heads and hydraulic conductivities (*K*). These parameters are critical to estimating groundwater flow, although there is an inherent difficulty in obtaining reliable *K* values in complex sedimentary environments (Rehfeldt et al., 1992). Local-scale *K* is obtained from grain size distributions across a shore-normal transect and slug tests performed on each piezometer, while site-scale parameters are derived from observations in groundwater level response to ocean tides.

3.3.1 | Grain size distribution of surficial materials to estimate local *K*

In the absence of core typically recovered from drilling boreholes, our study leverages grain size analyses and laboratory porosity measurements of surficial sediments of the WRD as one means to estimate hydraulic parameters. Nine sediment samples were collected over a 720 m transect perpendicular to the shoreline at equal intervals, beginning 50 m landward of Pz2 and ending at the beach face. The samples were collected between 20 and 30 cm depth of the depositional environment using a handheld trowel. Gradation analysis of each sample is determined optically at the University of Massachusetts Amherst Sediment and Coastal Dynamics Lab using a Camsizer (Retsch Technology, Germany) with a measurement range between 63 and 20 mm. Grains larger than 20 mm were removed, along with organic debris. Each cleaned bulk sample was dried in an oven before measurements were made. Due to our samples' wide range of grain sizes, we analysed at least 200 g from each. The hydraulic conductivity of each sample is estimated using empirical methods that fit the applicability requirements to relate grain size distribution with *K* (Table S3). The Hazen, USBR, Beyer, Kozeny–Carman, Terzaghi and Slitcher methods were selected for this determination (Beyer, 1964; Carman, 1956, 1997; Hazen, 1892; Kozeny, 1927, 1953; Slichter, 1899; Terzaghi et al., 1996; Vuković & Soro, 1992). We estimate the bulk porosity of samples in a laboratory setting using a 1000 mL graduated cylinder, which is first partially filled with a known volume of water. The sediment is added carefully to the cylinder and given time to settle and compact. The estimated porosity is determined by dividing the water volume by the sediment volume.

3.3.2 | Borehole scale analysis of *K*

After the installation and development of our piezometers, a series of falling head slug tests were conducted on 13 October 2021, 21 April 2022, 18 May 2023 and 19 September 2023 to determine the local saturated hydraulic conductivity (K_{sat}). Each piezometer was equipped with a Solinst Levelogger pressure transducer to measure water level every second during the slug tests. Once the water levels in the piezometers were at an equilibrium, the piezometer was quickly filled to the top of the casing with water. We observed steady-state conditions between subsequent slug tests, visually confirming the asymptotes in the water level data. Mean K_{sat} were calculated from the falling water levels using the Hvorslev's (Hvorslev, 1951), Bouwer-Rice (Bouwer & Rice, 1976) and KGS (Hyder et al., 1994) methods in the AQTESOLV 4.5 software.

3.3.3 | Tidal methods to characterize *K* at the site scale

Coastal aquifer systems experience periodic fluctuations in their groundwater levels due to propagating pressure waves induced by oscillations in the hydraulic head at the submarine boundary. In unconfined aquifers such as the WRD, this observed fluctuation emanates from changes in storage due to the dewatering and filling of the aquifer's pore space. As these pressure waves propagate inland, they attenuate and experience phase shifts, typically dampening out after several 100 m (Lanyon et al., 1982). At our experimental sites, semidiurnal and diurnal tidal signals are rarely observed in the time series of groundwater levels due to their proximity to the shoreline (>550 m). However, we observed a clear correlation between longer-period tidal fluctuations controlled by spring-neap-tidal cycles and the groundwater levels recorded in Pz2. These fluctuations were analysed with tidal response techniques to estimate hydraulic parameters over a larger scale. Aquifer diffusivity, the ratio of transmissivity to the storage coefficient, was calculated in the subaerial domain of the WRD using two direct methods that relate time series of tide levels to corresponding time series of groundwater levels at our tide-effected site (Pz2).

Although more complex approaches exist (Zhang et al., 2021), we obtained hydraulic diffusivity estimates from the tidal efficiency and time lag methods based on the well-established Ferris (1952) approaches, which offer simple, preliminary means to estimate aquifer parameters. The tidal efficiency of a coastal aquifer is defined as the ratio of the amplitude of groundwater fluctuations observed in a well to the amplitude of tidal fluctuations at the ocean boundary. The amplitude of the semidiurnal tidal fluctuation in the ocean-level data has essentially been attenuated completely, and only the lower frequency fluctuation remains. Therefore, the input time series for the

ocean water level was obtained by applying a running average of the difference between the high and low tides to create a self-similar signal with amplitudes that are representative of the spring-neap tide variability. The second direct method we apply to our time series data to calculate aquifer diffusivities is the time lag method. Theoretically, the time lag is the inverse of the velocity of the pressure wave's propagation as it moves through the aquifer. In simpler terms, it is subtracting the time of a peak or trough in the tidal time series from the corresponding peak or trough in the groundwater time series, which is how we estimate this parameter in the current study.

The methods described in the previous sections provide K as the estimated aquifer parameter. The diffusivity estimations from the tidal response methods must be converted to K to compare aquifer parameters determined through the three approaches we applied. The relationship between diffusivity (D) and hydraulic conductivity (K) in unconfined aquifer systems is given by:

$$K = \frac{DS_y}{b}, \tag{1}$$

where b is the saturated thickness of the aquifer at the location of groundwater level observations [m], and S_y is the aquifer's specific yield. We apply the estimation of aquifer thickness, b, from the HVSR results at Pz2 (49 m), discussed in the geophysical methods section. Concerning the aquifer's specific yield, S_y, we apply a value of 0.15. This is the median value for the representative range (0.1–0.2) of proglacial fans and sandur aquifers (Parriaux & Nicoud, 1990) and is the same calibrated value that was determined for an analogous site in a previous investigation (Mackay et al., 2020). We analysed 19 half cycles between 20 October 2021 and 25 May 2022. The dominant frequency determined by a fast Fourier transform of the well and ocean-level time series was used as the input tidal period for both the tidal efficiency and time lag methods (14.7 days).

3.4 | Geochemical characterization

Water samples were collected at each piezometer and the Wosnesenski stream site monthly to bi-monthly during the Alaskan field season (April–October). Samples were collected in clean 1-litre high-density polyethylene bottles. Pore water samples were collected using a peristaltic pump (Geopump, Geotech Environmental Equipment, Inc.) with clean tygon tubing. Bottles were rinsed three times with sample water before containing the sample. Before collecting the sample from the piezometers, we pumped at least three times the volume of water in the well to ensure that samples were derived from inflowing water across the well screen. Water samples for stable water isotopes and major elemental analysis were filtered with 0.45 μm PTFE membrane filters.

Water samples were analysed for δ^2H and $\delta^{18}O$ using a Picarro L-1102i WS-CRDS analyser (Picarro, Sunnyvale, CA) in the ENRI Stable Isotope Laboratory at the University of Alaska Anchorage. International reference standards (IAEA, Vienna, Austria) were used to calibrate the instrument to the VSMOW-VSLAP scale and working standards (USGS45: $\delta^2H = -10.3$ ‰, $\delta^{18}O = -2.24$ ‰ and USGS46: $\delta^2H = -235.8$ ‰, $\delta^{18}O = -29.8$ ‰) were used with each analytical run to correct for instrumental drift. Long-term mean and standard deviation records of a purified water laboratory internal QA/QC standard ($\delta^2H = -149.80$ ‰, $\delta^{18}O = -19.68$ ‰) yield an instrumental precision of 0.93 ‰ for δ^2H and 0.08 ‰ for $\delta^{18}O$.

Major elements were analysed at SGS Environmental Services in Lakefield, Ontario. Alkalinity was measured in the field using Chemetrics Titrets 10–100 ppm total alkalinity kits. Anions were analysed by ion chromatography following the methods in EPA300/MA300-inos1.3. Inductively coupled plasma mass spectrometry (ICP-MS) was used for elemental analysis using SM 3030/EPA 200.8 methods. All elemental analytical errors were reported to be less than 10%. The HCO_3^- and CO_3^{2-} concentrations were calculated using Geochemist's Workbench Community Edition 17.0 based on the alkalinity and pH of each sample. In this study, we report the sum of Ca, K, Mg, Na, HCO_3^-, SO_4^{2-}, Cl^- and SiO_2 as total dissolved solids (TDS) to compare our results with previous efforts.

4 | RESULTS

4.1 | Geophysical characterization results

4.1.1 | Resistivity profiles

The inverted resistivity profiles from our ERT surveys are presented in Figure 2. The first panel provides a shore-normal profile captured at high tide, the second panel provides the same profile at low tide, the third panel takes the difference between low and high tide (low—high) at the shore-normal transect, and the fourth panel provides the second transect parallel to the ocean at low tide. An inset map to the right of the first panel displays the relative location of electrodes along both transects. An additional inset to the right of the third panel provides an ocean water level time series of the day data were collected. The obtained results showed inverted bulk resistivities ranging from 1.0 to 373.7 Ωm and 0.7 to 414.2 Ωm for the shore-normal transect at high and low tide, respectively. The average inverted resistivities for the shore-normal transect were relatively similar for the high and low tides at 56.8 and 54.4 Ωm, respectively. Inverted resistivities for the transect parallel to the shore ranged from 0.3 to 265.9 Ωm, averaging 20.4 Ωm. The low inversion error (RMS) between 3.53% and 6.5% for all transects indicates that we achieved accurate and reliable results.

Assuming that aquifer levels are consistent with those observed in Pz2 across the transect, variation in resistivity due solely to changes in sediment facies may be detected in the upper 2–3 m of our profiles. In this case, the highest resistivity values (up to 374 Ωm) are observed in the pea gravel found on an active berm proximal to the bay, while the lowest resistivity values (7–20 Ωm) are observed in an intermittent tidal channel behind the berm dominated by finer sand. By assuming a limited variation in the sands and gravels that dominate

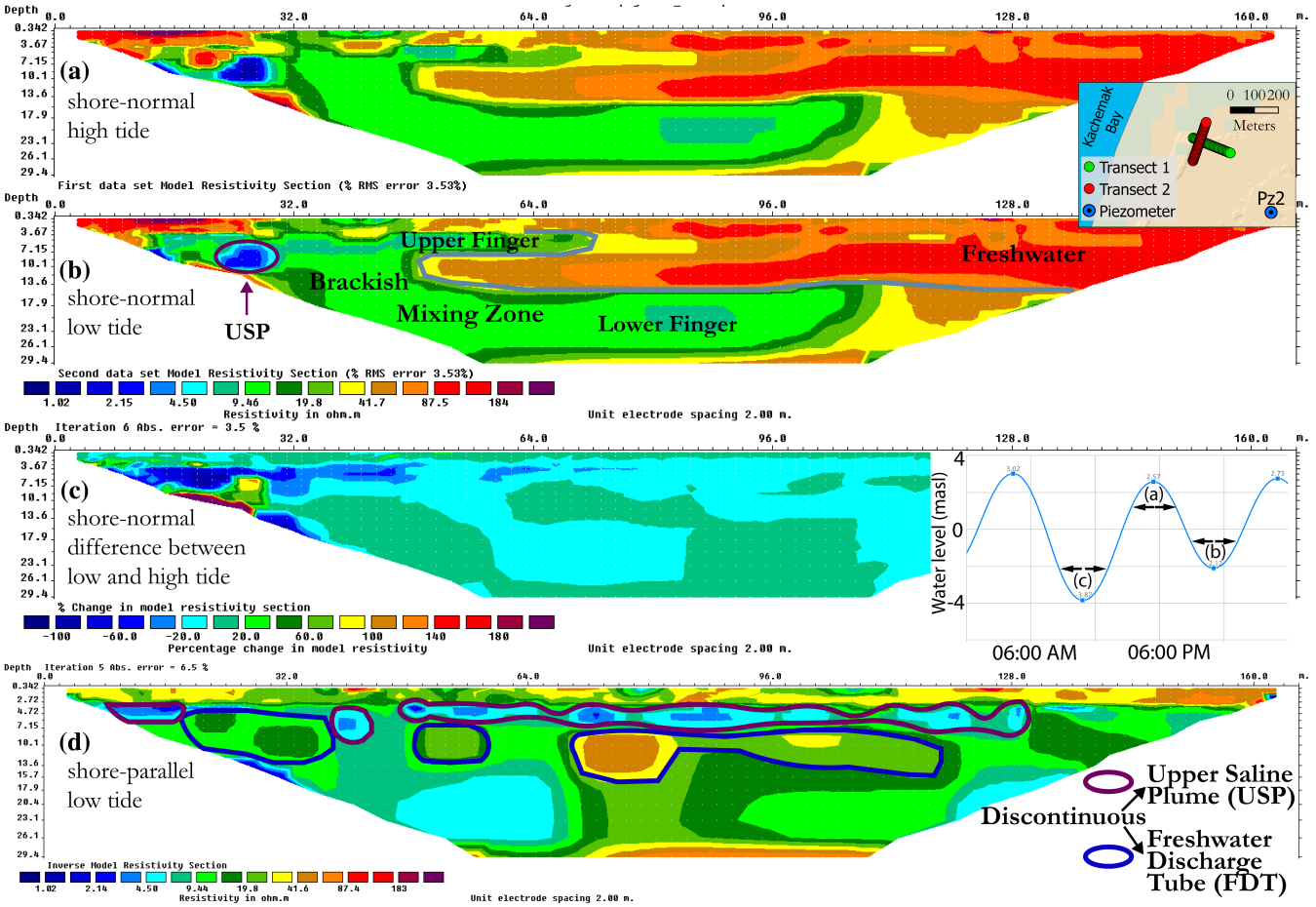

FIGURE 2 Sequence of inverted model bulk resistivities of field experimental data from 7 July 2020. (a) And (b) provide longshore transects at high and low tide, respectively, (c) takes the difference between high and low tide, and (d) provides a shore-parallel transect taken at low tide. Transects in plain view are provided in an inset map to the right of panel (a). Tide water levels from the day of data collection are provided in an inset time series to the right of panel (c); this inset has panels labelled over the time when each panel's data were collected. The freshwater-brackish water interface is delineated with a grey line in (b) and zones discussed in the text are labelled. The discontinuous upper saline plume (USP) and freshwater discharge tube are outlined in (d).

the WRD and assuming a low resistivity of seawater (0.1–5 Ωm due to the relative fresher seawater observed in Kachemak Bay), we may begin to delineate zones of freshwater, seawater and brackish water within this STE. Another benefit of performing a time-lapse is that variability between tides can be completely attributed to changes in the salinity of the groundwater.

Within the saturated zone of both transects, freshwater is observed as locations with higher resistivity (>32 Ωm; yellow-red). At both high and low tide in the shore-normal transects, freshwater occurs from 60 m inland to the end of the transect to a depth of 14 m below the ground surface (Figure 2a,b). Brackish water, the mixing zone between fresh and saltwater, is assumed to have intermediate resistivity values (5–32 Ωm; teal-green). The brackish water in the shore-normal transect protrudes into the coastal aquifer in two distinct fingers, one from 3 to 7 m of depth extending 72 m from the shoreline and the other from 16 to 30 m of depth extending 110 m inland (Figure 2a,b). These two fingers are connected vertically at a distance of 30–48 m from the shoreline. Both of the freshwater-brackish water interfaces are nearly horizontal, which is expected when groundwater levels, recharge rates and influx to the WRD aquifer are relatively low during summer conditions. We would expect this interface to be steeper if we performed this survey during spring months when aquifer levels and recharge rates are at their annual maxima.

Inland zones of freshwater and brackish water experienced little change throughout a tidal cycle (Figure 2c), except in a zone between 37–46 m inland and 2.2–4.5 m depth. Resistivity values increased by over 80% in this zone during the high tide transect (Figure 2c), indicating water with a higher freshwater content than that at low tide. Although this may seem counterintuitive, these results highlight the usefulness of our time-lapse in isolating preferential SGD zones. The ERT transects take approximately 195 min and work from electrode pairing to electrode pairing, beginning with those closest to the shore. We began collecting data for the high tide transect 95 min before the high tide, which means data collected at the zone of higher freshwater content was around 46 min before the high tide.

Groundwater with higher freshwater content is still discharging to the northern boundary at this time before infiltrating seawater is once again able to push it back during peak tidal conditions. Figure 2c highlights preferential fresh SGD pathways discharging to the northern boundary as inland zones with a high percent change in the profile.

The greatest changes in resistivity values over the tidal cycle are observed from near the shoreline to approximately 32 m inland below a depth of 2.5 m. The results obtained from our ERT transects delineate several classic features that are ubiquitous in the literature concerning STEs. The most prominent feature is the upper saline plume (USP; Robinson et al., 2006), which is between 5.6 and 11.2 m deep from 22 to 29 m inland (Figure 2a,b). The USP is formed from tidal recirculation along the sloping beach face and experiences the highest salinity during peak tidal conditions before mixing with discharging fresher water during low tide. Figure 2d images the variable distribution of the USP parallel to the shoreline that occurs due to preferential pathways that infiltrating seawater takes arising from variations in the permeability of the subsurface media. Below the USP, freshwater typically exits the STE in a freshwater discharge tube (FDT) that is confined between the USP and the saltwater wedge (Robinson et al., 2006). The variable distribution of the FDT is readily apparent in our transect parallel to the shore (Figure 2d) while remaining difficult to interpret in our shore-normal transects due to the truncation of the profile depth at the transect margins. In Figure 2d, brackish water discharging from the STE at low tide is imaged between depths of 5.4 and 17.0 m below the ground surface. Higher resistivity values indicative of relatively fresher water are readily apparent in the centre of this transect. This may be due to preferential flow pathways or due to the timing of electrode pairings in the transect, where data from the centre of the transect were collected during peak low tide conditions. The FDT is not continuous in the shore-normal transect due to the tide propagating from the northern boundary, which likely pushes the fresher water farther to the south. The saltwater wedge from this northern boundary is thought to be observed below the FDT on the left side of Figure 2d. We choose not to discuss significant differences observed in the shore-normal transects over the tidal cycle below the USP due to the possibility of errors or edge artefacts associated with a 2D resistivity tomogram (Hung et al., 2019).

4.1.2 | HVSR data

The calibration curve for Southcentral Alaska was composed of nine calibration stations (Table S1, Figure S1). The current study collected data at 12 sites with a range of sediment thicknesses necessary to calibrate the wide range of sediment thicknesses present in our study area. Three of these sites were removed due to data quality issues or undependable information from the well driller's logs. Thornley et al. (2021) provide resonance frequency peaks from 34 HVSR stations across the Municipality of Anchorage. We attempted to correlate their data with proximal bedrock-penetrating wells, though we were only able to use one of their sites due to either a well's proximity to their stations or because many of the wells in the area do not reach the bedrock surface within well driller's logs. The resulting power-law regression equation for Southcentral Alaska is given by:

$$H = 62.3 \times {f_0}^{-0.6914}, \quad (2)$$

where H = sediment thickness (m), f_0 = site resonance frequency (Hz) and the empirical constants represent the intercept and slope of the regression equation. Our equation is very different from other commonly used empirical equations (e.g., Haefner et al., 2010; Lane Jr et al., 2008), highlighting local calibration as an essential step when utilizing the HVSR method in new geographic settings. Calculated depths of our calibration stations had an average difference from the depths recorded by concurrent well driller's logs of 24%, with an R^2 of 0.83. This is within a reasonable bound of error, especially when considering the complex geologic history of the area and the reliability of well driller's logs.

Following the development of our correlation equation, unconsolidated sediment thicknesses within the WRD were estimated using the peak resonance frequency at 24 sites distributed across the delta (Figure 3). The calculated thicknesses ranged from 19 to 84 m spread across a 6 km transect from Kachemak Bay to the head of the delta. The acquired data has a reasonable distribution of sediment thickness. For example, stations near bedrock outcrops yield thinner sediment estimations than those that are more distal from outcrops. Another prevalent pattern is that the thickness of unconsolidated sedimentary deposits generally increases with stations that are closer to the ocean. Figure 3b provides a cross-section of a bedrock surface that slopes gently into Kachemak Bay, which we derive from our results. The average bedrock elevation at our sites is 41 m below sea level (Table S2). The thickest sediment was measured within the bedrock valley of the Wosnesenski River. Figure 3c renders a cross-section of an incised bedrock that occurred before the subsequent filling of the glaciofluvial valley.

4.2 | Hydraulic characterization results

4.2.1 | Estimation of *K* from grain size analysis

Delta plain surficial sediment samples of the WRD consist mostly of medium to coarse sands and gravels (Figure 4). The average effective particle size (d_{10}) across all samples is 0.345 mm, indicative of medium sands. The cumulative weight percentage of sediments with particle diameter <2.0 mm is more than 50% at eight out of the nine sites, with site SS1 being the only one that is predominately composed of fine gravel. The porosity of samples ranges from 0.26 to 0.37, with an average of 0.32. The uniformity coefficient (Cu) of samples ranges from 2.4 to 16.5, with an average of 7.8. Samples SS5, SS7 and SS8 are classified as well-sorted, while the rest are poorly to very poorly sorted. Porosity generally increases with closer proximity to the coast, while Cu generally decreases in the same direction.

The average hydraulic conductivity values (K) computed across the six statistical grain size methods ranged from 5 to 129 m d^{-1}, with a mean value from all sediment samples of 39 m d^{-1} (Table S4).

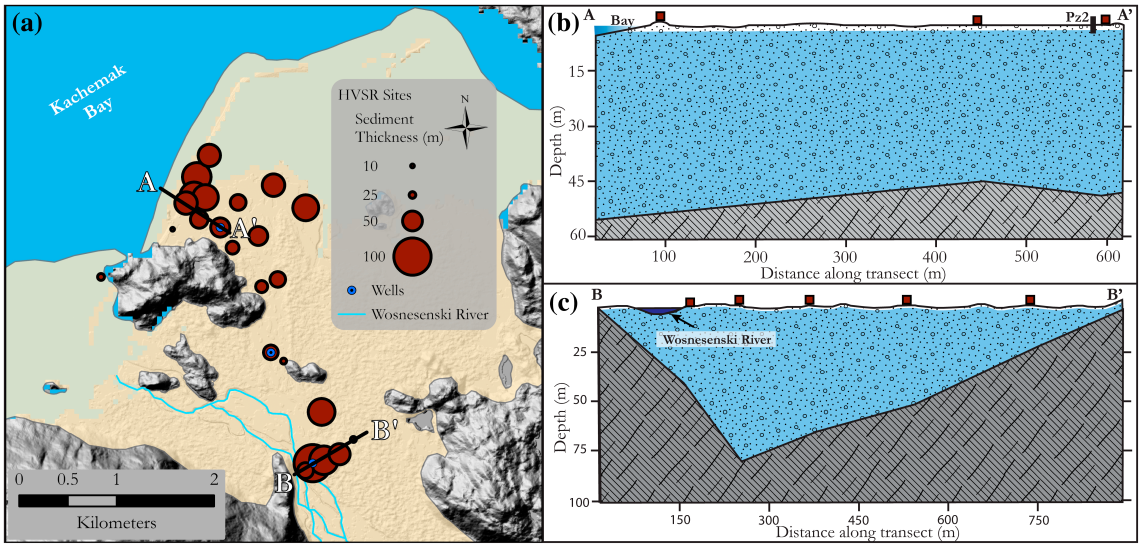

FIGURE 3 (a) Map providing the locations of HVSR data collected within the WRD. Symbol sizes are proportional to the unconsolidated surficial sediment thicknesses estimated for each site; (b) and (c) are example cross-sections constructed from estimated thicknesses, with the areal extent of transect lines provided in (a). Red squares on (b) and (c) mark HVSR survey locations. HVSR, horizontal-to-vertical spectral ratio; WRD, Wosnesenski River Delta.

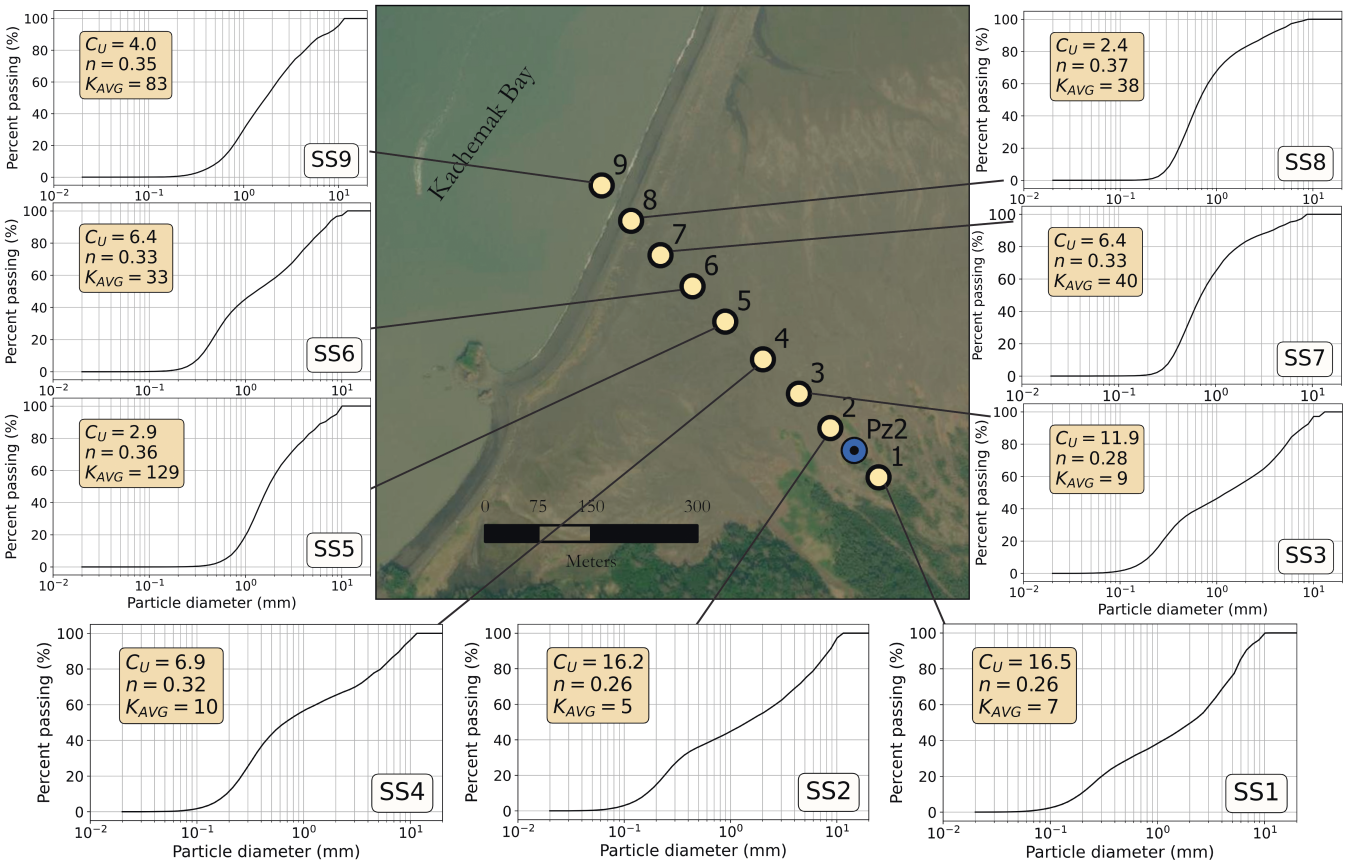

FIGURE 4 Map of sediment sample collection in the WRD with grain size distribution plots for all samples. Each plot additionally provides the coefficient of unconformity (Cu), porosity (n) and average hydraulic conductivity (K_{avg}) from empirical equations. WRD, Wosnesenski River Delta.

Estimates of *K* provided by the USBR and Terzaghi methods consistently calculated values lower than the other methods, while the Beyer method always calculated the highest, when applicable, and also had the highest range between samples. The relative standard error of the mean between methods is 61% and is observed to increase with increasing Cu ($R^2 = 0.66$). The Terzaghi and Slitcher

methods were the only relationships that could be applied to each sample according to the domain of applicability requirements for the empirical methods (Table S3). One sediment sample does not apply to the Beyer method due to a high effective particle size, five sediment samples do not apply to the USBR method due to high uniformity coefficients, and the majority of samples do not apply to Kozeny–Carman and Hazen approximations due to small effective particle sizes and high uniformity coefficients, respectively. Spatial variability in grain size distributions and the average K across applicable methods is provided in Figure 4.

4.2.2 | Estimation of K from slug tests

The slug test-derived average hydraulic conductivity (K) along the piezometer transect ranged from 2 to 27 m d^{-1}, also indicative of medium to coarse sands (Table 1). The relative standard error of the mean between methods for each test ranged from 2% to 16%, with a mean of 6%. The consistently lowest estimates were obtained from Pz2, the piezometer that is the farthest down gradient and closest to Kachemak Bay. The highest variability of K values was observed in Pz1, which is set in the margins of a modern braid bar of the Wosnesenski River. Slug tests performed on 13 October 2021 and 21 April 2022 at this site returned the same average value for K of 3 m d^{-1}. During slug tests performed on 20 May 2023 and 20 September 2023, the average K at Pz1 increased to 29 and 48 m d^{-1}, respectively. This increase coincides with the active cutting of the braid bar from channel migration during high-water events in 2022 and 2023. During this time, the active mobilization of fine sediments within the hyporheic zone likely led to this observed increase in K (Stewardson et al., 2016).

4.2.3 | Estimation of K from tidal methods

Time series datasets used for the tidal methods are provided in Figure 5. The tidal level time series is characterized by the largest amplitudes and shows mixed character in both semidiurnal and spring-neap cycles. The low-frequency ocean level amplitude associated with spring-neap-tidal cycles had an average amplitude of 2.5 m (SD = 0.7 m). The piezometric time series of Pz2 had an average amplitude of 0.6 m (SD = 0.2). The time lag between peaks and troughs of the low-frequency ocean level and aquifer level data was 2.7 days (SD = 0.2 days).

Aquifer diffusivities and the corresponding hydraulic conductivities based on the tidal efficiency and time lag methods are provided in Table S5. Calculated diffusivities use a depth of 48.9 m at Pz2, as determined in the previous geophysical results section. The average tidal amplitude and time lag diffusivity estimates for the analysis period overviewed in Figure 3 are 34 119 and 50 408 m^2 d^{-1}, respectively (Figure 1). After applying a conservative value for specific yield (0.15), average values for K were 105 and 155 m d^{-1} for the tidal efficiency and time lag methods, respectively (Table 1). Significant variability using data collected at different dates has been noted previously in the literature (Águila et al., 2023; Jha et al., 2008). However, both methods provided a sensible range of estimates for the highly conductive media of the WRD across dates.

4.3 | Geochemical characterization results

Ionic concentrations and stable water isotopic compositions from our 2-year geochemical sampling campaign are given in Figure 6. Each sampling location has a unique symbol, the colour of which is dictated by the month that the sample was collected (Figure 6). Major ions are plotted against Cl^- concentrations, a conservative tracer that has been commonly applied to assess the distribution of travel times from multiple water source end-members and pathways within a catchment (Cox et al., 2007; Hoeg et al., 2000; Kirchner et al., 2010; Rice & Hornberger, 1998). Samples collected from Pz2, our groundwater site that is the farthest down gradient, show less variability in Cl^- concentrations than the other sites. The river site and the more proximal wells show a similar pattern of decreasing Cl^- concentrations during the glacial melt season (July–September), which is generally, when peak flows, occur on the Wosnesenski River. This indicates significant

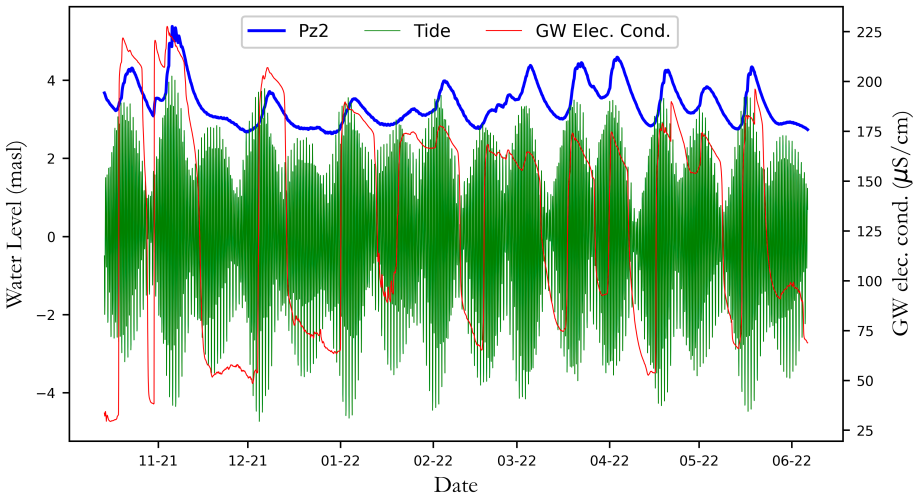

FIGURE 5 Time series observations of groundwater and tide water levels (meters above sea level) and groundwater electrical conductivity (µS/cm). Groundwater level and electrical conductivity observations were collected from our Pz2 site, while tide levels were provided by the Seldovia, AK station (https://tidesandcurrents.noaa.gov/waterlevels.html?id=9455500; last accessed on 26 October 2023).

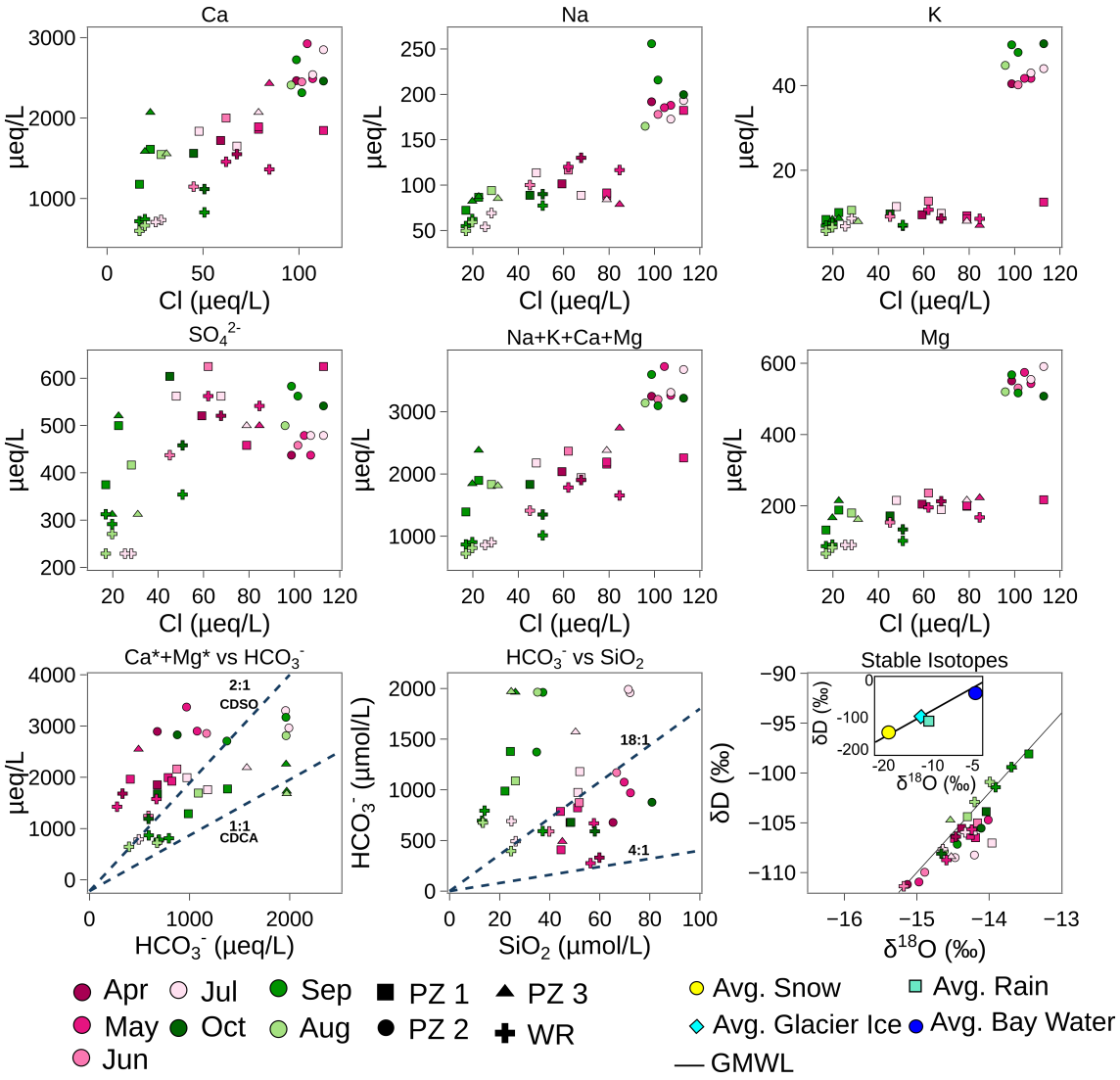

FIGURE 6 Geochemical characterization of sampled shallow groundwater and river water within the WRD across seasons. The colour of data represents the month sampled and shapes refer to our four experimental site locations. Relationships of major ions with chloride are provided, as well as a plot of stable isotopes. The $\delta^{18}O$ versus δD values of average rain, snow, glacier and seawater collected over 5 years are provided in the inset in the stable isotopes plot. The brown oval within this inset provides the location of our data. CDCA, carbonate dissolution via carbonic acid; CDSO, carbonate dissolution via sulphide oxidation; WRD, Wosnesenski River Delta; an * indicates that concentrations were corrected for precipitation.

stream water exchange with the proximal groundwaters during this time. The river samples and Pz2, the coastal piezometer, provide two generalized end-members within this system. Pz2 represents a cumulative mix of flow paths and transit times, whereas the river is driven by shorter transit times and less interaction with geologic media on its path, particularly during the melt season. By plotting major ions against Cl^-, viewers may qualitatively and visually separate out the catchment storage timescales within, with higher Cl^- concentrations representing a larger spectrum of water age, pathways, and sources that reach each site. If separate lines are drawn between river samples and Pz2 for each month, then samples from Pz1 and Pz3 should fall within that mixing line and in that order. Points above and below these lines indicate enrichment or depletion, respectively, by chemical reactions and/or cation exchange. This is indeed the case for our samples, particularly during the meltwater season (Figure 6). In these samples, major cations show that enrichment of groundwaters proximal to the river occurs during the primary melt season (July–September), while samples are slightly depleted during baseflow conditions. One must also consider the potential lag time that occurs between sites. Pz1, located 112 m from the river, is likely influenced by river water much more rapidly than Pz3, which is located 630 m from the river. This lag time is readily apparent during July when samples from Pz1 move toward the river water end-member a month earlier than those from Pz3. Our monthly sampling plan also highlights the importance of collecting samples across seasons since end-members in this dynamic environment change frequently.

Water types for the shallow groundwater of our well sites and the Wosnesenski River are classified using a Piper diagram (Figure S2). The samples mainly fall within the Ca-HCO_3 type, except for a few samples from the Wosnesenski River and wells closer to the river (Pz1 and Pz3) which tend toward the Ca-SO_4 type earlier in the year before the onset of the melt season (April or May). This follows a clear pattern observable in Figure 6, where concentrations of SO_4^{2-} and HCO_3^- for the Wosnesenski River and its proximal piezometers show opposite trends across hydrologic seasons. Between spring baseflow conditions and the peak meltwater season (July/August), SO_4^{2-} concentrations are reduced by 41%–60% at all three sites. The opposite trend occurs for HCO_3^-, with concentrations increasing by 290%–402% at the same sites. This observation does not hold at Pz2, where both SO_4^{2-} and HCO_3^- concentrations increase by 167% and 402% through the summer, respectively.

5 | DISCUSSION

Our integrative approach provides multiple insights into the workings of coastal groundwater systems along the GoA margin, which may be broadened to other high-latitude coastal margins. In this section, we compare and synthesize observations made in the results section to highlight the key aspects of this system's physical and chemical functioning and provide an upscaled Darcy flux estimate for the WRD.

5.1 | Aquifer delineation through geophysical examination

Describing the boundary conditions within an aquifer is requisite for studies concerning the subsurface. By deploying geophysical techniques, key components of the coastal aquifer of the WRD were delineated. The ERT transect was particularly useful in identifying locations of subterranean estuarine dynamics within the near-shore environment, including a distinct brackish water wedge protruding into the aquifer system at distances of at least 110 m from the coastline. Inverted resistivity values also allowed for the identification of two brackish water-freshwater interfaces. The occurrence of two distinct freshwater-brackish water interfaces could occur due to several reasons. First, the distribution of mixing water within the subsurface may be predominately controlled by heterogeneity coupled with tidal range, as similar structures have been simulated in 2D numerical flow models (Geng et al., 2020; Li et al., 2009, 2016). Additionally, the two interfaces could be due to the tidal propagation of seawater from two directions at the location of our transects. The closest oceanic boundary to the west may be responsible for the deeper, thicker brackish water finger protruding into the WRD aquifer, while the shallow, thinner finger may result from the tidal propagation from the north where seawater travels up to 2 km over the intertidal zone. Seawater derived from the northern tidal propagation has been observed to enter the subsurface in concentrated recharge pathways at the end of tidal channels.

The ERT results also successfully defined the locations of both the surficial mixing zone of the USP and the freshwater discharge tube, which occur between depths of 5.6–11.2 m and 5.4–17.0 m, respectively. Cross-shore variability, as shown through a time-lapse of high and low tides (Figure 2a,b), reveals these zones' dynamic flow and transport behaviour. Very few studies have successfully mapped USPs, even fewer in locations with such a high tidal range (Grünenbaum et al., 2023; LeRoux et al., 2023). To the best of our knowledge, we are the first to delineate a large USP in the GoA driven by these high tidal oscillations. This feature is likely a major portion of the total SGD flux and is an important biogeochemical hotspot within the STE. Additionally, this delineation provides beneficial guidance for future experimental designs. It is also crucial to set up initial conditions and calibrate and validate subsequent numerical simulations of groundwater dynamics within the aquifer.

The usefulness of passive seismic techniques to rapidly estimate sediment thicknesses within these coastal aquifer systems is also presented in this study. The bedrock boundary is an essential piece of information required for estimations of storage and flux in proglacial aquifer systems. Classical approaches to estimate sediment thicknesses in proglacial environments typically involve imaging the subsurface through electrical resistivity or seismic refraction profiling (Guðmundsson et al., 2002; Müller et al., 2022), which are substantially more time consuming and costly with excessive equipment requirements. The development of the first HVSR calibration curve for Southcentral Alaska highlights that a site's resonance frequency within this area varies considerably from depths calculated in previous work in distant geographic locations. An average thickness of 49 m was calculated from 24 stations within the WRD. This considerable thickness brings additional prominence to the storage and geochemical reaction potential within. Although this is a meaningful start, additional calibration points are required to add to the robustness of the current calibration curve. Additional points are also necessary if we proceed to extrapolate a sediment thickness map encompassing the entirety of the WRD for a 3D simulation. Many of these areas remain difficult to access, and a large population of bears prevented mobility within a sizeable area in the northeastern portion of the delta. Additionally, concurrent stations would further resolve the reliability of this approach.

5.2 | Hydraulic parameterization over multiple scales of inquiry reveals congruent estimations

One of the greatest challenges of characterizing the hydrogeology of a study area is appropriately determining aquifer parameters, such as hydraulic conductivity. We deployed several empirical and hydraulic methods that vary from sample to field in scale, all of which are neither costly nor time-consuming to perform. Each method provides K estimates spanning 1–2 orders of magnitude. However, the mean results from different methods are within a reasonable difference from one another (same order of magnitude). Slug tests performed in piezometers provided the lowest range of results, while the direct

tidal methods estimated the highest average values. This follows the consensus where previous investigations reported increasing K over larger scales (Fallico et al., 2010; Hunt, 2006; Schulze-Makuch et al., 1999).

The average aquifer diffusivity calculated by the time lag method was 50 400 m d^{-1}, which is over 16 000 m d^{-1} than those calculated by the tidal efficiency method (Table S5). Previous studies have noted similar dissimilarities (Águila et al., 2023; Jha et al., 2008; Sánchez-Úbeda et al., 2018). Jha et al. (2008) recommended that the time lag method should only be applied for a rough estimation of aquifer parameters as it consistently yielded very large hydraulic diffusivity values that varied considerably across sites. Inconsistencies between the tidal efficiency and time lag method have been investigated in depth by Trefry and Bekele (2004). Their results indicate the tidal efficiency-based diffusivity estimates as more reliable. Variability in both the time lag and tidal efficiency methods may be attributed to several factors that substantially influence the results when calculating parameters using data from different dates. For simplicity, the theoretical solutions we apply only consider one tidal component with idealized, steady-state boundary conditions, and that diffusivity does not vary with fluctuations in the water table height as the partial differential equation is assumed to be linear. Additional processes that contribute to the variability between tidal efficiency and time lag methods include a sloped aquifer base (Su et al., 2003) and the difference in the propagation of water table fluctuations as a function of the ratio of the wave period to the aquifer depth (Nielsen et al., 1997; Shoushtari et al., 2016). Environmental conditions, such as barometric pressure, wind speed, water temperature and recharge conditions resulting from snow melt and rain, may also influence the tidal wave propagation through the WRD aquifer. For example, Wunsch and Stammer (1997) describe an oceanic 'inverted barometer' effect that will cause a variation of 1.02 cm in sea level for a fluctuation of 1 mbar in atmospheric pressure, and Guimond et al. (2023) found the dominant mechanism of aquifer recharge and groundwater discharge to be wind-driven. We provide a plot of atmospheric pressure, average daily temperature and daily precipitation in Figure S3 to cater the visualization of the dynamic relations between aquifer levels and environmental forces. To help reduce this uncertainty, we use the geometric mean across different dates ($n = 19$ for reliable peaks and troughs) over a longer, continuous dataset.

The results from the tidal efficiency method are regarded as the most useful since it captures the greatest extent of the aquifer and is within a reasonable range of both the grain size analyses and the slug tests. Additional advantages of this method are that it provides a representative combined description of aquifer properties over a large spatial scale from a single point measurement and helps resolve issues over the spatial variabilities in aquifer systems that may not be determined by the other methods. Previous work in geologic analogues assigned specific yields on the higher end of our range, typically from 0.15 to 0.25 for sands and gravels (Chen et al., 2010; Mackay et al., 2020; Müller et al., 2023; Nilsson et al., 2007). Further, this technique may also be applied to estimate K near the Wosnesenski River based on the diurnal flood-wave response observed in proximal piezometers during the melt season or after significant rain events. We deployed a sensor into the Wosnesenski River that was buried during meltwater floods in 2022 and remains unrecovered.

Numerous efforts have promoted the necessity to utilize multiple means for the estimation of K since a sole method appropriate for all geological media does not exist, and unguided choices can lead to large errors in this parameter estimation (Águila et al., 2023; Hwang et al., 2017; Mohanty et al., 1994). By deploying these multiple lines of inquiry, we have begun to define this system as highly permeable with strong connectivity between marine and terrestrial domains. We find that all of the methods applied provide reasonable estimates for the hydraulic conductivity of the WRD, which may be implemented at similar sites across the GoA margin and other analogous high-latitude coastal aquifer systems. Müller et al. (2022) compiled a review of hydraulic conductivity values reported in proglacial studies. They provide a range of 10–657 m d^{-1} for K (mean across studies = 142 m d^{-1}) in analogous geologic landforms (e.g., outwash plains).

5.3 | A geochemical perspective of coastal groundwater in Alaska

Our geochemical investigation in the WRD provided leading evidence for the significance of coastal groundwaters within the GoA. Most importantly, these waters are considerably enriched in nutrients and solutes when compared to the proximal river samples, regardless of season (Figure 6). This is congruent with the overwhelming consensus in the literature concerning SGD globally (Connolly et al., 2020; Rodellas et al., 2015; Santos et al., 2021; Swarzenski et al., 2007; Taniguchi et al., 2019). Elemental concentrations of major ions measured within our coastal piezometer, Pz2, were up 7.2× greater than those measured from river samples. A substantial enrichment was observed in nearly every analyte we examined across seasons, except for SO_4^{2-} before the onset of the melt season (April–May samples). One must also consider that our samples only describe the shallow groundwater chemistry. Martínez-Pérez et al. (2022) provide findings that concentrations of major ions increase significantly with depth in their study site. Additionally, we observe that this enrichment occurs along a gradient, with concentrations increasing with increasing proximity to the coast, suggesting that the length of flow-path and water–rock interactions are important.

Geochemical results indicate high connectivity between the Wosnesenski River and the adjacent aquifer system over large spatial scales. Pz3 is located in an abandoned river channel 630 m from the river. In dynamic deltaic systems such as the WRD, abandoned channels are widely distributed and occur at many depths. These high-energy depositional environments offer effective conduits that have the potential to rapidly route water out of the stream and transport it quickly over large distances, increasing the water's nutrient and solute concentrations along the way. We observe waters derived from snow and glacier melt within the river that travels 630 m from the stream to Pz3. This change in groundwater composition occurs within a month of when the river chemistry shifts, illustrating once again the highly

conductive nature of the aquifer. These observations indicate that concentrated aquifer recharge occurs over the river corridor during the meltwater season. Similar recharge processes have been observed in other glacierized streams. Liljedahl et al. (2017) calculated that an Alaskan headwater stream in the Yukon River drainage basin lost between 38% and 56% of its annual streamflow to recharge lowland aquifers. The authors attempted to explain long-term increases in lowland river baseflow due to this phenomenon. Similarly, Ó Dochartaigh et al. (2019) demonstrated active aquifer recharge from river losses through tracer data in a proglacial outwash plain in Iceland, and subsequent studies found that focused infiltration will become an even larger source of groundwater recharge with current climate change projections (Mackay et al., 2020). In coastal aquifers, this concentrated recharge may be a mechanism to enhance fresh SGD rates to marine environments. However, knowledge concerning how climate change and glacier recession will affect these coastal aquifers and SGD rates is limited.

Several seasonal patterns are observed in Figure 6. Winnick et al. (2017) describe in detail the direct control of snowmelt on the anion concentration hysteresis that is recognized in our data. Briefly, lower groundwater levels during periods dominated by baseflow allow oxidized waters to more readily pass through the pyrite oxidation front where sulphuric acid is neutralized by HCO_3^- and rapidly deprotonates to SO_4^{2-}, thus increasing its concentration while removing alkalinity (Kemeny et al., 2021; Winnick et al., 2017). This effect experiences a strong dilution during periods of rising water tables associated with the meltwater season. The different pattern observed in the seasonal fluctuation of SO_4^{2-} with groundwater at Pz2 is due simply to the timing of peak groundwater levels at this location, which occurs in March–April from the melting of the low-elevation snowpack (Figure 6). The SO_4^{2-} concentration at this site increases with declining water table heights observed during summer months, providing sustained concentrations while river exports are at a minimum.

5.4 | Synthesis of findings, upscaling of Darcy flux calculations and recommended additions for successive investigations

Insights gained through this investigation are summarized within a conceptual model of the hydrogeochemical functioning of the WRD in Figure 7. This conceptual model illustrates the complex but consistent stream-aquifer-oceanic interactions that were observed over the two-year field campaign. The application of methods across three branches of hydrogeology yields a more complete perspective of these intimate connections: (1) geophysics delineated the structure of the aquifer system through which the interactions occur and defined zones of highly dynamic salinity patterns across tidal cycles, (2) hydraulic methods supply physical parameterization of the geologic media and reveal rapid responses between terrestrial and oceanic forces and (3) hydrochemistry of the Wosnesenski River and its proximal shallow groundwater featured a close and active connection

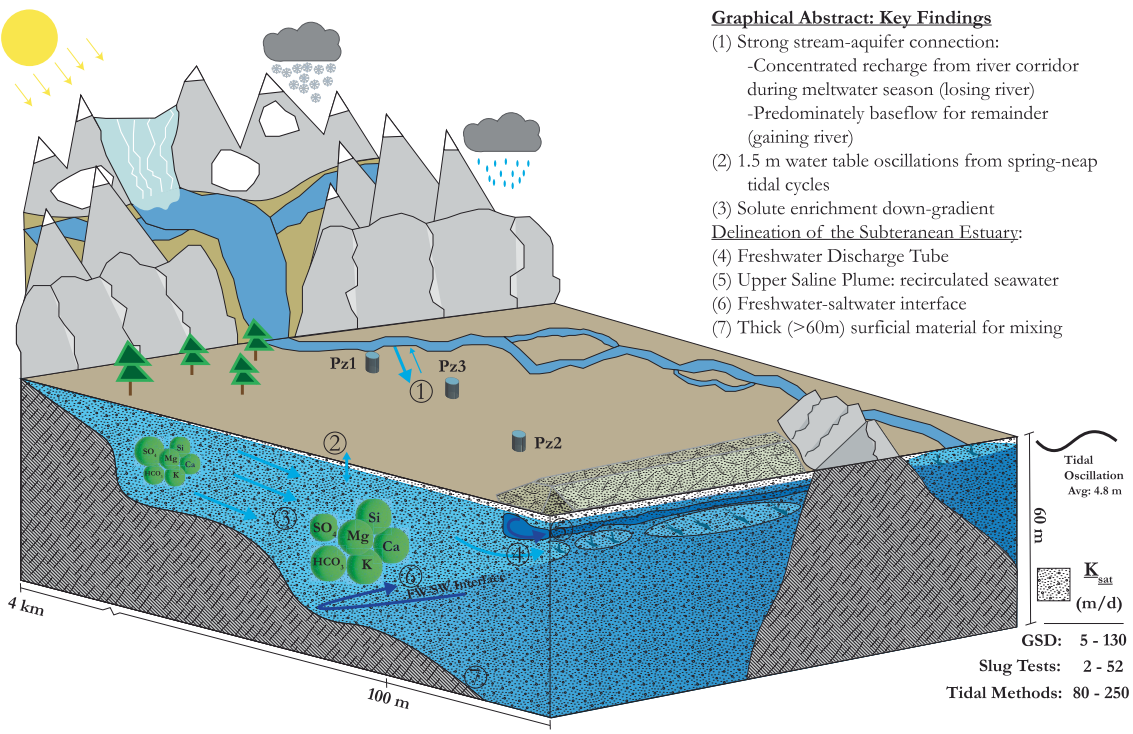

FIGURE 7 Graphical abstract summarizing the major findings from our experimental field site in the Wosnesenski River Delta. Circled numbers provided in the depiction are explained in corresponding numbers listed in the text. The range of saturated hydraulic conductivities, K_{sat}, from different methods is presented in the lower right-hand side (GSD, grain size distribution).

between stream and aquifer processes that are supported by the hydraulic parameterization. Although these methods are impractical to achieve at a larger regional scale, the findings can be applied across the GoA coastal margin in a more generalized sense. Thousands of similar deltas occur along this margin and are likely to experience similar connectivity with adjacent reservoirs and enriched chemical concentrations. Additionally, our findings may be used to inform future investigations in both the WRD as well as the greater GoA region and other coastlines globally. Lastly, our investigation into this system provides a baseline characterization that may be compared to future studies that may observe alterations that occur with the current radical land cover change.

The hydrochemical and hydraulic techniques we applied resulted in congruent findings that further confirm the major aquifer interactions. Our observations expose the necessity for geochemical sampling across seasons and spatial areas to observe the connectedness of coastal aquifer systems to adjacent surface water bodies. The groundwater chemistry near the river followed similar patterns as the meltwater during the summer months, and this relationship reversed outside of the meltwater season (Figure 4). Groundwater solute concentrations become enriched with distance from the river, typically reaching the highest observed elemental concentrations in our sampling location closest to the ocean. A strong hydraulic connectivity between the freshwater aquifer system and the ocean was also observed through our groundwater monitoring, where up to nearly 2 m oscillations occur due to spring and neap-tidal cycles over distances of at least 550 m.

This synthesis of approaches enables a preliminary estimation of the freshwater and solute flux delivered to the marine environment from the WRD through an upscaling application of Darcy's Law. By combining the bulk hydraulic conductivity from hydraulic methods ($K = 105$ m d^{-1}, mean value from tidal efficiency model), the average hydraulic gradient between aquifer and ocean water levels calculated through groundwater monitoring (0.006), the average sediment thickness of the coastline estimated through geophysical methods (55 m) and the average TDS measured through geochemical sampling (180 mg/L), these estimates may be readily made along the 6150 m coast of the WRD outside of the Wosnesenski watershed. We approximate fresh SGD from the WRD to an average of 2.5 m^3 s^{-1} with a daily yield of 39 tonnes of dissolved solutes. This estimate does not account for the solute enrichment or depletion that may occur in the STE between Pz2 and the coast. Further, this estimate does not include the flux from delta sediments beneath the modern Wosnesenski River.

In a recent study, Russo et al. (2023) estimated the mean annual flux of fresh, terrestrial groundwater to the GoA to be 3.5%–11.4% of the total freshwater flux (combined rivers and fresh SGD). Results from their study provide fresh SGD estimates from the WRD to average around 24 700 m^3 d^{-1}, equivalent to 0.29 m^3 s^{-1}. The estimate provided by the current study is nearly an order of magnitude higher over the same area. Russo et al. (2023) were also unable to quantify the influence of streams on coastal catchments, which our current study has found to be a significant source of recharge. Although both values are significantly less than the average flux delivered from the Wosnesenski River of 32 m^3 s^{-1} during the melt season (Jenckes et al., 2023), the enhanced solute chemistry of this groundwater system emphasizes the importance of coastal groundwaters to the biogeochemistry of Kachemak Bay. Jenckes et al. (2023) estimated the TDS flux from the Wosnesenski River during the melt season to be 210 tonnes day^{-1}. Our estimation of the average dissolved solute flux from the aquifer is 19% across the same period, and fresh SGD likely dominates this flux outside of the melt season. We have observed the Wosnesenski River in both dry and frozen conditions during this time, while groundwater levels within Pz2 remain relatively consistent, suggesting a sustained contribution of freshwater and solutes throughout the year. Assuming these concentrations reflect mean values, input from coastal groundwater has the potential to rival the input from rivers within the GoA. Further, we sample groundwater from the upper portion of the WRD aquifer, which may not be representative of enriched solute concentrations that may occur at depth.

Monitoring efforts identified high variability in the hydraulic gradient between Pz2 and the coast, ranging from less than zero during flood tides occurring in the days before peak spring-tide conditions to 0.016 during ebb tides in the days following peak spring-tide conditions (Figure 3). This observation indicates that the delivery of fresh SGD to the coast has significant temporal variability and exposes the days following peak spring tidal cycles as times of significant groundwater flushing to the near-shore environment and the ecosystems within. This monitoring also highlighted consistent groundwater levels throughout the year, and maintained moderate levels through the winter months when the river flux is near zero.

The conceptual model of the WRD would benefit from several additions to provide a more thorough representation of this system. While shallow piezometers are simple and economical to instal, deeper penetrating wells would provide further insight into the stratigraphy and hydrochemistry of the WRD aquifer. Additional piezometers distributed throughout the domain would further aid in an accurate delineation of the water table and allow for observations of any substantial variabilities in processes that may have been overlooked. The experimental set-up of Martínez-Pérez et al. (2022) included 13 boreholes, nine of which were grouped in three nests, which allowed for the discovery of an aquifer that behaved as a multi-aquifer system previously thought to behave as one cohesive unit. Our conceptualization would also benefit greatly from the addition of a river gauge, allowing the direct comparison of river levels with proximal groundwater levels. Additionally, the hydraulic diffusivity of the near-river aquifer system may be estimated through the direct tidal methods that we used at Pz2.

6 | CONCLUSIONS

This study developed a more detailed understanding of coastal unconfined aquifer systems of the GoA margin and integrated several disciplines to characterize a locally connected system from a physical and chemical perspective. The quantitative and geochemical analyses are

simple and are based on the hydraulic and geochemical responses observed within the WRD. Even so, the integrative framework captured a broad view of the dynamic stream-aquifer-oceanic continuum and is readily transferable to subsequent studies and regions. The findings presented here emphasize the benefits of using an integrated approach across disciplines to assess aquifer processes and interactions at a catchment scale.

Hydraulic conductivities obtained from multiple lines of inquiry and at multiple scales repeatedly supported the highly permeable nature of these environments. The site instrumentation and tidal response analyses featured a strong connection between marine and terrestrial forces. Geochemical sampling revealed coastal groundwaters as significantly enriched in nutrients and solutes across seasons compared to the proximal river concentrations. These samples also highlighted a clear connection between the river and aquifer systems, with concentrated recharge occurring over the river corridor during the meltwater season. This recharge travels long distances over short periods, experiencing geochemical enrichment along its path. Geophysical techniques allowed the delineation of key features within the STE and estimated sediment thicknesses that average 49 m over a 6 km long transect.

The methods in this study are informative, low-cost, and readily applicable to catchment-scale hydrogeologic investigations in mountainous coastal areas across the GoA and other coastal margins globally. They may be particularly useful in remote sites where access and mobility are challenging, as exemplified within the WRD. Improved characterization of coastal aquifers is needed to guide effective water resource management decisions and project future climate change-driven alterations, particularly in the GoA. Kachemak Bay is one of the most productive estuaries in the world. Developing a thorough understanding of SGD is essential for the protection of the coastal ecosystem, as well as for its cultural and economic importance.

DATA AVAILABILITY STATEMENT

The data that support the findings of this study are openly available in ScholarWorks@UA at https://scholarworks.alaska.edu/handle/11122/14902.

ORCID

A. A. Russo https://orcid.org/0000-0002-9756-0156

D. F. Boutt https://orcid.org/0000-0003-1397-0279

REFERENCES

Adams, P. N., Ruggiero, P., Schoch, G. C., & Gelfenbaum, G. (2007). Intertidal sand body migration along a megatidal coast, Kachemak Bay, Alaska. *Journal of Geophysical Research: Earth Surface*, *112*, F02007.

Águila, J. F., McDonnell, M. C., Flynn, R., Butler, A. P., Hamill, G. A., Etsias, G., Benner, E. M., & Donohue, S. (2023). Comparison of saturated hydraulic conductivity estimated by empirical, hydraulic and numerical modeling methods at different scales in a coastal sand aquifer in Northern Ireland. *Environmental Earth Sciences*, *82*, 327.

Alorda-Kleinglass, A., Ruiz-Mallén, I., Diego-Feliu, M., Rodellas, V., Bruach-Menchén, J. M., & Garcia-Orellana, J. (2021). The social implications of submarine groundwater discharge from an ecosystem services perspective: A systematic review. *Earth-Science Reviews*, *221*, 103742.

Anderson, S. P. (2005). Glaciers show direct linkage between erosion rate and chemical weathering fluxes. *Geomorphology*, *67*, 147–157.

Bard, P., & Participants, S. (2004). The SESAME project: an overview and main results, 1–6.

Beamer, J. P., Hill, D. F., Mcgrath, D., Arendt, A., & Kienholz, C. (2017). Hydrologic impacts of changes in climate and glacier extent in the G ulf of a laska watershed. *Water Resources Research*, *53*, 7502–7520.

Bergstrom, A., Koch, J. C., O'Neel, S., & Baker, E. (2021). Seasonality of Solute Flux and Water Source Chemistry in a Coastal Glacierized Watershed Undergoing Rapid Change: Wolverine Glacier Watershed, Alaska. *Water Resources Research*, *57*, e2020WR028725.

Beyer, W. (1964). Zur bestimmung der wasserdurchlässigkeit von kiesen und sanden aus der kornverteilungskurve. *Wasserwirtschaft Wassertechnik*, *14*, 165–168.

Bieniek, P. A., Walsh, J. E., Thoman, R. L., & Bhatt, U. S. (2014). Using climate divisions to analyze variations and trends in Alaska temperature and precipitation. *Journal of Climate*, *27*, 2800–2818.

Bouraoui, F., Vachaud, G., Li, L., Le Treut, H., & Chen, T. (1999). Evaluation of the impact of climate changes on water storage and groundwater recharge at the watershed scale. *Climate Dynamics*, *15*, 153–161.

Bouwer, H., & Rice, R. (1976). A slug test for determining hydraulic conductivity of unconfined aquifers with completely or partially penetrating wells. *Water Resources Research*, *12*, 423–428.

Bradley, D. C., Kusky, T. M., & Ford, A. (1992). Deformation history of the McHugh complex, Seldovia quadrangle, south-central Alaska. *US Geological Survey Bulletin*, *1999*, 17–32.

Burke, J. J., & Moench, M. H. (2000). Groundwater and society: resources, tensions and opportunities. Themes in groundwater management for the twenty-first century: Department of International Economic and Social Affairs, Statistical Office ….

Burnett, W. C., Bokuniewicz, H., Huettel, M., Moore, W. S., & Taniguchi, M. (2003). Groundwater and pore water inputs to the coastal zone. *Biogeochemistry*, *66*, 3–33.

Burnett, W. C., Santos, I. R., Weinstein, Y., Swarzenski, P. W., & Herut, B. (2007). Remaining uncertainties in the use of Rn-222 as a quantitative tracer of submarine groundwater discharge. *IAHS Publication*, *312*, 109.

Carman, P. C. (1956). Flow of gases through porous media: (No title).

Carman, P. C. (1997). Fluid flow through granular beds. *Chemical Engineering Research and Design*, *75*, S32–S48.

Chen, X., Song, J., & Wang, W. (2010). Spatial variability of specific yield and vertical hydraulic conductivity in a highly permeable alluvial aquifer. *Journal of Hydrology*, *388*, 379–388. https://doi.org/10.1016/j.jhydrol.2010.05.017

Clark, S. H., & Geological Survey (Estados Unidos), and Government Printing Office. (1973). *The McHugh complex of south-central Alaska*. US Government Printing Office.

Connolly, C. T., Cardenas, M. B., Burkart, G. A., Spencer, R. G., & McClelland, J. W. (2020). Groundwater as a major source of dissolved organic matter to Arctic coastal waters. *Nature Communications*, *11*, 1479.

Coulter, H. W., & Migliaccio, R. R. (1966). *Effects of the earthquake of march 27, 1964, at Valdez* (Vol. 542). US Government Printing Office.

Cox, M. H., Su, G. W., & Constantz, J. (2007). Heat, chloride, and specific conductance as ground water tracers near streams. *Groundwater*, *45*, 187–195.

Crusius, J., Schroth, A. W., Gassó, S., Moy, C. M., Levy, R. C., & Gatica, M. (2011). Glacial flour dust storms in the Gulf of Alaska: Hydrologic and meteorological controls and their importance as a source of bioavailable iron. *Geophysical Research Letters*, *38*, L06602.

Daigle, T. A., & Kaufman, D. S. (2009). Holocene climate inferred from glacier extent, lake sediment and tree rings at goat lake, Kenai Mountains, Alaska, USA. *Journal of Quaternary Science: Published for the Quaternary Research Association*, *24*, 33–45.

Diego-Feliu, M., Rodellas, V., Alorda-Kleinglass, A., Saaltink, M., Folch, A., & Garcia-Orellana, J. (2022). Extreme precipitation events

induce high fluxes of groundwater and associated nutrients to coastal ocean. *Hydrology and Earth System Sciences*, *26*, 4619–4635.

Dimova, N. T., Swarzenski, P. W., Dulaiova, H., & Glenn, C. R. (2012). Utilizing multichannel electrical resistivity methods to examine the dynamics of the fresh water–seawater interface in two Hawaiian groundwater systems. *Journal of Geophysical Research: Oceans*, *117*, C02012.

Döll, P., Hoffmann-Dobrev, H., Portmann, F. T., Siebert, S., Eicker, A., Rodell, M., Strassberg, G., & Scanlon, B. R. (2012). Impact of water withdrawals from groundwater and surface water on continental water storage variations. *Journal of Geodynamics*, *59*, 143–156.

Fallico, C., De Bartolo, S., Troisi, S., & Veltri, M. (2010). Scaling analysis of hydraulic conductivity and porosity on a sandy medium of an unconfined aquifer reproduced in the laboratory. *Geoderma*, *160*, 3–12.

Fellman, J. B., Hood, E., Raymond, P. A., Hudson, J., Bozeman, M., & Arimitsu, M. (2015). Evidence for the assimilation of ancient glacier organic carbon in a proglacial stream food web. *Limnology and Oceanography*, *60*, 1118–1128.

Ferris, J. G. (1952). Cyclic fluctuations of water level as a basis for determining aquifer transmissibility: US geological survey.

Geng, X., Michael, H. A., Boufadel, M. C., Molz, F. J., Gerges, F., & Lee, K. (2020). Heterogeneity affects intertidal flow topology in coastal beach aquifers. *Geophysical Research Letters*, *47*, e2020GL089612.

Grünenbaum, N., Günther, T., Greskowiak, J., Vienken, T., Müller-Petke, M., & Massmann, G. (2023). Salinity distribution in the subterranean estuary of a meso-tidal high-energy beach characterized by electrical resistivity tomography and direct push technology. *Journal of Hydrology*, *617*, 129074.

Guðmundsson, M. T., Bonnel, A., & Gunnarsson, K. (2002). Seismic soundings of sediment thickness on Skeiðarársandur, SE Iceland. *Jökull*, *51*, 53–64.

Guimond, J. A., Demir, C., Kurylyk, B. L., Walvoord, M. A., McClelland, J. W., & Cardenas, M. B. (2023). Wind-modulated groundwater discharge along a microtidal Arctic coastline. *Environmental Research Letters*, *18*, 094042.

Guimond, J. A., Mohammed, A. A., Walvoord, M. A., Bense, V. F., & Kurylyk, B. L. (2022). Sea-level rise and warming mediate coastal groundwater discharge in the Arctic. *Environmental Research Letters*, *17*, 045027.

Haag, J., Dulai, H., & Burt, W. (2023). The role of submarine groundwater discharge to the input of macronutrients within a macrotidal subpolar estuary. *Estuaries and Coasts*, *46*, 1740–1755.

Haefner, R. J., Sheets, R. A., & Andrews, R. E. (2010). Evaluation of the horizontal-to-vertical spectral ratio (HVSR) seismic method to determine sediment thickness in the vicinity of the south well field, Franklin County, OH. *Ohio Journal of Science*, *110*(4), 77–85.

Hajati, M., Sutanudjaja, E., & Moosdorf, N. (2019). Quantifying regional fresh submarine groundwater discharge with the lumped modeling approach CoCa-rfsgd. *Water Resources Research*, *55*, 5321–5341.

Hallet, B., Hunter, L., & Bogen, J. (1996). Rates of erosion and sediment evacuation by glaciers: A review of field data and their implications. *Global and Planetary Change*, *12*, 213–235.

Hauri, C., Schultz, C., Hedstrom, K., Danielson, S., Irving, B., Doney, S. C., Dussin, R., Curchitser, E. N., Hill, D. F., & Stock, C. A. (2020). A regional hindcast model simulating ecosystem dynamics, inorganic carbon chemistry, and ocean acidification in the Gulf of Alaska. *Biogeosciences*, *17*, 3837–3857.

Hawkings, J. R., Benning, L. G., Raiswell, R., Kaulich, B., Araki, T., Abyaneh, M., Stockdale, A., Koch-Müller, M., Wadham, J. L., & Tranter, M. (2018). Biolabile ferrous iron bearing nanoparticles in glacial sediments. *Earth and Planetary Science Letters*, *493*, 92–101.

Hazen, A. (1892). *Physical properties of sands and gravels with reference to their use infiltration: Massachusetts state Board of Health*. Mass.

Hoeg, S., Uhlenbrook, S., & Leibundgut, C. (2000). Hydrograph separation in a mountainous catchment—Combining hydrochemical and isotopic tracers. *Hydrological Processes*, *14*, 1199–1216.

Hood, E., & Berner, L. (2009). Effects of changing glacial coverage on the physical and biogeochemical properties of coastal streams in southeastern Alaska: Journal of geophysical research. *Biogeosciences*, *114*, G03001.

Hood, E., Fellman, J. B., & Spencer, R. G. M. (2020). Glacier loss impacts riverine organic carbon transport to the ocean. *Geophysical Research Letters*, *47*, e2020GL089804.

Hood, E., & Scott, D. (2008). Riverine organic matter and nutrients in southeast Alaska affected by glacial coverage. *Nature Geoscience*, *1*, 583–587.

Hung, Y.-C., Lin, C.-P., Lee, C.-T., & Weng, K.-W. (2019). 3D and boundary effects on 2D electrical resistivity tomography. *Applied Sciences*, *9*, 2963.

Hunt, A. (2006). Scale-dependent hydraulic conductivity in anisotropic media from dimensional cross-over. *Hydrogeology Journal*, *14*, 499–507.

Huss, M., & Hock, R. (2018). Global-scale hydrological response to future glacier mass loss. *Nature Climate Change*, *8*, 135–140.

Hvorslev, M. J. (1951). *Time lag and soil permeability in ground-water observations: Waterways Experiment Station*. Corps of Engineers, US Army.

Hwang, H.-T., Jeen, S.-W., Suleiman, A. A., & Lee, K.-K. (2017). Comparison of saturated hydraulic conductivity estimated by three different methods. *Water*, *9*, 942.

Hyder, Z., Butler, J. J., Jr., McElwee, C. D., & Liu, W. (1994). Slug tests in partially penetrating wells. *Water Resources Research*, *30*, 2945–2957.

Ibs-von Seht, M., & Wohlenberg, J. (1999). Microtremor measurements used to map thickness of soft sediments. *Bulletin of the Seismological Society of America*, *89*, 250–259.

Jakob, L., Gourmelen, N., Ewart, M., & Plummer, S. (2021). Spatially and temporally resolved ice loss in High Mountain Asia and the Gulf of Alaska observed by CryoSat-2 swath altimetry between 2010 and 2019. *The Cryosphere*, *15*, 1845–1862.

Jenckes, J., Ibarra, D. E., & Munk, L. A. (2022). Concentration-discharge patterns across the Gulf of Alaska reveal geomorphological and Glacierization controls on stream water solute generation and export. *Geophysical Research Letters*, *49*, e2021GL095152.

Jenckes, J., Munk, L., Ibarra, D., Boutt, D., Fellman, J., & Hood, E. (2023). Hydroclimate drives seasonal riverine export across a gradient of Glacierized high-latitude coastal catchments. *Water Resources Research*, *59*, e2022WR033305.

Jha, M. K., Namgial, D., Kamii, Y., & Peiffer, S. (2008). Hydraulic parameters of coastal aquifer systems by direct methods and an extended tide–aquifer interaction technique. *Water Resources Management*, *22*, 1899–1923.

Johannesson, K. H., Palmore, C. D., Fackrell, J., Prouty, N. G., Swarzenski, P. W., Chevis, D. A., Telfeyan, K., White, C. D., & Burdige, D. J. (2017). Rare earth element behavior during groundwater–seawater mixing along the Kona coast of Hawaii. *Geochimica et Cosmochimica Acta*, *198*, 229–258.

Johnson, M. A. (2021). Subtidal surface circulation in lower cook inlet and Kachemak bay, Alaska. *Regional Studies in Marine Science*, *41*, 101609.

Kemeny, P. C., Lopez, G. I., Dalleska, N., Torres, M., Burke, A., Bhatt, M., West, A. J., Hartmann, J., & Adkins, J. (2021). Sulfate sulfur isotopes and major ion chemistry reveal that pyrite oxidation counteracts CO2 drawdown from silicate weathering in the Langtang-Trisuli-Narayani River system Nepal Himalaya. *Geochimica et Cosmochimica Acta*, *294*, 43–69.

Kim, G., Ryu, J.-W., Yang, H.-S., & Yun, S.-T. (2005). Submarine groundwater discharge (SGD) into the Yellow Sea revealed by 228Ra and 226Ra isotopes: Implications for global silicate fluxes. *Earth and Planetary Science Letters*, *237*, 156–166.

Kirchner, J. W., Tetzlaff, D., & Soulsby, C. (2010). Comparing chloride and water isotopes as hydrological tracers in two Scottish catchments. *Hydrological Processes*, *24*, 1631–1645.

Knee, K., & Paytan, A. (2011). Submarine groundwater discharge: A source of nutrients, metals, and pollutants to the Coastal Ocean. *Treatise on Estuarine and Coastal Science*, *4*, 205–234.

Kozeny, J. (1927). Ueber kapillare leitung des wassers im boden. *Sitzungsberichte der Akademie der Wissenschaften in Wien*, *136*, 271.

Kozeny, J. (1953). Das wasser im boden. Grundwasserbewegung. *Hydraulik: Ihre Grundlagen Und Praktische Anwendung*, 380–445.

Kroeger, K. D., Swarzenski, P. W., Greenwood, W. J., & Reich, C. (2007). Submarine groundwater discharge to Tampa Bay: Nutrient fluxes and biogeochemistry of the coastal aquifer. *Marine Chemistry*, *104*, 85–97.

Kundzewicz, Z. W., & Doell, P. (2009). Will groundwater ease freshwater stress under climate change? *Hydrological Sciences Journal*, *54*, 665–675.

Kurtz, B. E., Landmeyer, J. E., & Culter, J. K. (2023). Precipitation, submarine groundwater discharge of nitrogen, and red tides along the southwest Florida Gulf coast. *Heliyon*, *9*, e16046.

Kusky, T. M., & Bradley, D. C. (1999). Kinematic analysis of mélange fabrics: Examples and applications from the McHugh complex, Kenai peninsula, Alaska. *Journal of Structural Geology*, *21*, 1773–1796.

Kwon, E. Y., Kim, G., Primeau, F., Moore, W. S., Cho, H., DeVries, T., Sarmiento, J. L., Charette, M. A., & Cho, Y. (2014). Global estimate of submarine groundwater discharge based on an observationally constrained radium isotope model. *Geophysical Research Letters*, *41*, 8438–8444.

Lane, J. W., Jr., White, E. A., Steele, G. V., & Cannia, J. C. (2008). Estimation of bedrock depth using the horizontal-to-vertical (H/V) ambient-noise seismic method. *Symposium on the Application of Geophysics to Engineering and Environmental Problems Proceedings*, *Society of Exploration Geophysicists*, Tulsa, USA, 490–502.

Lane, S. N., Bakker, M., Gabbud, C., Micheletti, N., & Saugy, J.-N. (2017). Sediment export, transient landscape response and catchment-scale connectivity following rapid climate warming and alpine glacier recession. *Geomorphology*, *277*, 210–227.

Lanyon, J., Eliot, I., & Clarke, D. (1982). Groundwater-level variation during semidiurnal spring tidal cycles on a sandy beach. *Marine and Freshwater Research*, *33*, 377–400.

Larsen, C. F., Motyka, R. J., Freymueller, J. T., Echelmeyer, K. A., & Ivins, E. R. (2004). Rapid uplift of southern Alaska caused by recent ice loss. *Geophysical Journal International*, *158*, 1118–1133.

Lecher, A. L., Mackey, K., Kudela, R., Ryan, J., Fisher, A., Murray, J., & Paytan, A. (2015). Nutrient loading through submarine groundwater discharge and phytoplankton growth in Monterey bay, CA. *Environmental Science & Technology*, *49*, 6665–6673.

Lecher, A. L., & Mackey, K. R. M. (2018). Synthesizing the effects of submarine groundwater discharge on marine biota. *Hydrology*, *5*, 60.

Lee, E., Yoon, H., Hyun, S. P., Burnett, W. C., Koh, D., Ha, K., Kim, D., Kim, Y., & Kang, K. (2016). Unmanned aerial vehicles (UAVs)-based thermal infrared (TIR) mapping, a novel approach to assess groundwater discharge into the coastal zone. *Limnology and Oceanography: Methods*, *14*, 725–735.

LeRoux, N., Frey, S., Lapen, D., Guimond, J., & Kurylyk, B. (2023). Megatidal and surface flooding controls on coastal groundwater and saltwater intrusion within agricultural Dikelands. *Water Resources Research*, *59*, e2023WR035054.

Li, X., Hu, B. X., Burnett, W. C., Santos, I. R., & Chanton, J. P. (2009). Submarine ground water discharge driven by tidal pumping in a heterogeneous aquifer. *Groundwater*, *47*, 558–568.

Li, X., Hu, B. X., & Tong, J. (2016). Numerical study on tide-driven submarine groundwater discharge and seawater recirculation in heterogeneous aquifers. *Stochastic Environmental Research and Risk Assessment*, *30*, 1741–1755.

Liljedahl, A., Gädeke, A., O'Neel, S., Gatesman, T., & Douglas, T. (2017). Glacierized headwater streams as aquifer recharge corridors, subarctic Alaska. *Geophysical Research Letters*, *44*, 6876–6885.

Lilkendey, J., Pisternick, T., Neumann, S. I., Dumur Neelayya, D., Bröhl, S., Neehaul, Y., & Moosdorf, N. (2019). Fresh submarine groundwater discharge augments growth in a reef fish. *Frontiers in Marine Science*, *6*, 613.

Loke, M., & Barker, R. (1995). Least-squares deconvolution of apparent resistivity pseudosections. *Geophysics*, *60*, 1682–1690.

Luo, X., & Jiao, J. J. (2016). Submarine groundwater discharge and nutrient loadings in Tolo Harbor, Hong Kong using multiple geotracer-based models, and their implications of red tide outbreaks. *Water Research*, *102*, 11–31.

Mackay, J. D., Barrand, N. E., Hannah, D. M., Krause, S., Jackson, C. R., Everest, J., MacDonald, A. M., & Ó Dochartaigh, B. É. (2020). Proglacial groundwater storage dynamics under climate change and glacier retreat. *Hydrological Processes*, *34*, 5456–5473.

Martínez-Pérez, L., Luquot, L., Carrera, J., Marazuela, M. A., Goyetche, T., Pool, M., Palacios, A., Bellmunt, F., Ledo, J., & Ferrer, N. (2022). A multidisciplinary approach to characterizing coastal alluvial aquifers to improve understanding of seawater intrusion and submarine groundwater discharge. *Journal of Hydrology*, *607*, 127510.

Michael, H. A. (2005). Seasonal dynamics in costal aquifers: Investigation of submarine groundwater discharge through field measurements and numerical models.

Michael, H. A., Lubetsky, J. S., & Harvey, C. F. (2003). Characterizing submarine groundwater discharge: A seepage meter study in Waquoit Bay, Massachusetts. *Geophysical Research Letters*, *30*(6), 1297.

Michael, H. A., Russoniello, C. J., & Byron, L. A. (2013). Global assessment of vulnerability to sea-level rise in topography-limited and recharge-limited coastal groundwater systems. *Water Resources Research*, *49*, 2228–2240.

Michael, H. A., Scott, K. C., Koneshloo, M., Yu, X., Khan, M. R., & Li, K. (2016). Geologic influence on groundwater salinity drives large seawater circulation through the continental shelf. *Geophysical Research Letters*, *43*, 10–782.

Mizukami, N., Newman, A. J., Littell, J. S., Giambelluca, T. W., Wood, A. W., Gutmann, E. D., Hamman, J. J., Gergel, D. R., Nijssen, B., Clark, M. P., & Arnold, J. R. (2022). New projections of 21st century climate and hydrology for Alaska and Hawai'i. *Climate Services*, *27*, 100312. https://doi.org/10.1016/j.cliser.2022.100312

Mohanty, B., Kanwar, R. S., & Everts, C. (1994). Comparison of saturated hydraulic conductivity measurement methods for a glacial-till soil. *Soil Science Society of America Journal*, *58*, 672–677.

Molnar, S., Cassidy, J., Castellaro, S., Cornou, C., Crow, H., Hunter, J., Matsushima, S., Sánchez-Sesma, F., & Yong, A. (2018). Application of microtremor horizontal-to-vertical spectral ratio (MHVSR) analysis for site characterization: State of the art. *Surveys in Geophysics*, *39*, 613–631.

Moore, W. S. (1996). Large groundwater inputs to coastal waters revealed by 226Ra enrichments. *Nature*, *380*, 612–614.

Moore, W. S. (1999). The subterranean estuary: A reaction zone of ground water and sea water. *Marine Chemistry*, *65*, 111–125.

Moore, W. S. (2010). The effect of submarine groundwater discharge on the ocean. *Annual Review of Marine Science*, *2*, 59–88.

Moosdorf, N., & Oehler, T. (2017). Societal use of fresh submarine groundwater discharge: An overlooked water resource. *Earth-Science Reviews*, *171*, 338–348.

Müller, T., Lane, S. N., & Schaefli, B. (2022). Towards a hydrogeomorphological understanding of proglacial catchments: An assessment of groundwater storage and release in an alpine catchment. *Hydrology and Earth System Sciences*, *26*, 6029–6054.

Müller, T., Roncoroni, M., Mancini, D., Lane, S. N., & Schaefli, B. (2023). Current and future role of meltwater-groundwater dynamics in a proglacial Alpine outwash plain. *EGUsphere*, 1–34. doi:10.5194/edushpere-2022-1503

Mulligan, A. E., & Charette, M. A. (2006). Intercomparison of submarine groundwater discharge estimates from a sandy unconfined aquifer. *Journal of Hydrology*, *327*, 411–425.

Mulligan, A. E., Evans, R. L., & Lizarralde, D. (2007). The role of paleochannels in groundwater/seawater exchange. *Journal of Hydrology*, *335*, 313–329.

Nakamura, Y. (1989). A method for dynamic characteristics estimation of subsurface using microtremor on the ground surface. *Railway Technical Research Institute, Quarterly Reports*, *30*(1).

Nielsen, P., Aseervatham, R., Fenton, J. D., & Perrochet, P. (1997). Groundwater waves in aquifers of intermediate depths. *Advances in Water Resources*, *20*, 37–43.

Nilsson, B., Højberg, A., Refsgaard, J., & Troldborg, L. (2007). Uncertainty in geological and hydrogeological data. *Hydrology and Earth System Sciences*, *11*, 1551–1561.

Ó Dochartaigh, B. É., MacDonald, A. M., Black, A. R., Everest, J., Wilson, P., Darling, W. G., Jones, L., & Raines, M. (2019). Groundwater–glacier meltwater interaction in proglacial aquifers. *Hydrology and Earth System Sciences*, *23*, 4527–4539.

O'Neel, S., Hood, E., Bidlack, A. L., Fleming, S. W., Arimitsu, M. L., Arendt, A., Burgess, E., Sergeant, C. J., Beaudreau, A. H., & Timm, K. (2015). Icefield-to-ocean linkages across the northern Pacific coastal temperate rainforest ecosystem. *Bioscience*, *65*, 499–512.

Paldor, A., Frederiks, R. S., & Michael, H. A. (2022). Dynamic steady state in coastal aquifers is driven by multi-scale cyclical processes, controlled by aquifer Storativity. *Geophysical Research Letters*, *49*, e2022GL098599.

Panthi, J., Johnson, C. D., Pradhanang, S. M., Savage, B., Ismail, M. Y., & Boving, T. B. (2023). Delineating bedrock topography with geophysical techniques: An implication for groundwater mapping. *Catena*, *230*, 107258.

Parriaux, A., & Nicoud, G. (1990). Hydrological behaviour of glacial deposits in mountainous areas. *Hydrology of Mountainous Areas*, *190*, 291–312.

Peng, T., Zhu, Z., Du, J., & Liu, J. (2021). Effects of nutrient-rich submarine groundwater discharge on marine aquaculture: A case in Lianjiang, East China Sea. *Science of the Total Environment*, *786*, 147388.

Prakash, R., Srinivasamoorthy, K., Gopinath, S., & Saravanan, K. (2018). Measurement of submarine groundwater discharge using diverse methods in Coleroon estuary, Tamil Nadu, India. *Applied Water Science*, *8*, 1–11.

Raiswell, R., Tranter, M., Benning, L. G., Siegert, M., De'ath, R., Huybrechts, P., & Payne, T. (2006). Contributions from glacially derived sediment to the global iron (oxyhydr) oxide cycle: Implications for iron delivery to the oceans. *Geochimica et Cosmochimica Acta*, *70*, 2765–2780.

Rehfeldt, K. R., Boggs, J. M., & Gelhar, L. W. (1992). Field study of dispersion in a heterogeneous aquifer: 3. Geostatistical analysis of hydraulic conductivity. *Water Resources Research*, *28*, 3309–3324.

Rice, K. C., & Hornberger, G. M. (1998). Comparison of hydrochemical tracers to estimate source contributions to peak flow in a small, forested, headwater catchment. *Water Resources Research*, *34*, 1755–1766.

Richardson, C., Davis, K., Ruiz-González, C., Guimond, J. A., Michael, H., Paldor, A., Moosdorf, N., & Paytan, A. (2024). The impacts of climate change on coastal groundwater. *Nature Reviews Earth & Environment*, *5*, 1–20.

Rienecker, M. M., Suarez, M. J., Gelaro, R., Todling, R., Bacmeister, J., Liu, E., Bosilovich, M. G., Schubert, S. D., Takacs, L., & Kim, G.-K. (2011). MERRA: NASA's modern-era retrospective analysis for research and applications. *Journal of Climate*, *24*, 3624–3648.

Robinson, C., Gibbes, B., Carey, H., & Li, L. (2007). Salt-freshwater dynamics in a subterranean estuary over a spring-neap tidal cycle. *Journal of Geophysical Research: Oceans*, 112. doi:10.1029/2006JC003888

Robinson, C., Gibbes, B., & Li, L. (2006). Driving mechanisms for groundwater flow and salt transport in a subterranean estuary. *Geophysical Research Letters*, *33*, L03402.

Robinson, C., Li, L., & Barry, D. A. (2007). Effect of tidal forcing on a subterranean estuary. *Advances in Water Resources*, *30*, 851–865.

Rocha, C., Veiga-Pires, C., Scholten, J., Knoeller, K., Gröcke, D. R., Carvalho, L., Anibal, J., & Wilson, J. (2016). Assessing land–ocean connectivity via submarine groundwater discharge (SGD) in the ria Formosa lagoon (Portugal): Combining radon measurements and stable isotope hydrology. *Hydrology and Earth System Sciences*, *20*, 3077–3098.

Rodellas, V., Garcia-Orellana, J., Masqué, P., Feldman, M., & Weinstein, Y. (2015). Submarine groundwater discharge as a major source of nutrients to the Mediterranean Sea. *Proceedings of the National Academy of Sciences*, *112*, 3926–3930.

Russo, A. A., Boutt, D. F., Munk, L. A., & Jenckes, J. (2023). Contribution of fresh submarine groundwater discharge to the Gulf of Alaska. *Water Resources Research*, *59*, e2023WR034912. https://doi.org/10.1029/2023WR034912

Sánchez-Úbeda, J. P., Calvache, M. L., López-Chicano, M., & Duque, C. (2018). The effects of non-tidal components, depth of measurement and the use of peak delays in the application of tidal response methods. *Water Resources Management*, *32*, 481–495.

Santos, I. R., Chen, X., Lecher, A. L., Sawyer, A. H., Moosdorf, N., Rodellas, V., Tamborski, J., Cho, H.-M., Dimova, N., & Sugimoto, R. (2021). Submarine groundwater discharge impacts on coastal nutrient biogeochemistry. *Nature Reviews Earth & Environment*, *2*, 307–323.

Schmoll, H. R., & Yehle, L. A. (1986). Pleistocene glaciation of the upper cook inlet basin.

Schroth, A. W., Crusius, J., Chever, F., Bostick, B. C., & Rouxel, O. J. (2011). Glacial influence on the geochemistry of riverine iron fluxes to the Gulf of Alaska and effects of deglaciation. *Geophysical Research Letters*, *38*, L16605.

Schulze-Makuch, D., Carlson, D. A., Cherkauer, D. S., & Malik, P. (1999). Scale dependency of hydraulic conductivity in heterogeneous media. *Groundwater*, *37*, 904–919.

Setiawan, B., Jaksa, M., Griffith, M., & Love, D. (2018). Estimating bedrock depth in the case of regolith sites using ambient noise analysis. *Engineering Geology*, *243*, 145–159.

Shanley, C. S., Pyare, S., Goldstein, M. I., Alaback, P. B., Albert, D. M., Beier, C. M., Brinkman, T. J., Edwards, R. T., Hood, E., & MacKinnon, A. (2015). Climate change implications in the northern coastal temperate rainforest of North America. *Climatic Change*, *130*, 155–170.

Shiklomanov, I. A., & Rodda, J. C. (2003). *World water resources at the beginning of the twenty-first century*. Cambridge University Press.

Sholkovitz, E., Herbold, C., & Charette, M. (2003). An automated dye-dilution based seepage meter for the time-series measurement of submarine groundwater discharge. *Limnology and Oceanography: Methods*, *1*, 16–28.

Shoushtari, S. M. H. J., Cartwright, N., Nielsen, P., & Perrochet, P. (2016). The effects of oscillation period on groundwater wave dispersion in a sandy unconfined aquifer: Sand flume experiments and modelling. *Journal of Hydrology*, *533*, 412–420.

Slichter, C. S. (1899). Theoretical investigation of the motion of ground waters. *The 19th Ann Rep. US Geophys Survey*, 304–319.

Slomp, C. P., & Van Cappellen, P. (2004). Nutrient inputs to the coastal ocean through submarine groundwater discharge: Controls and potential impact. *Journal of Hydrology*, *295*, 64–86.

Somers, L. D., & McKenzie, J. M. (2020). A review of groundwater in high mountain environments. *Wiley Interdisciplinary Reviews Water*, *7*, e1475.

Spalt, N., Murgulet, D., & Abdulla, H. (2020). Spatial variation and availability of nutrients at an oyster reef in relation to submarine groundwater discharge. *Science of the Total Environment*, *710*, 136283.

Stewardson, M., Datry, T., Lamouroux, N., Pella, H., Thommeret, N., Valette, L., & Grant, S. (2016). Variation in reach-scale hydraulic conductivity of streambeds. *Geomorphology*, *259*, 70–80.

Stieglitz, T. (2005). Submarine groundwater discharge into the near-shore zone of the great barrier reef, Australia. *Marine Pollution Bulletin*, *51*, 51–59.

Stieglitz, T., Rapaglia, J., & Bokuniewicz, H. (2008). Estimation of submarine groundwater discharge from bulk ground electrical conductivity measurements. *Journal of Geophysical Research: Oceans*, *113*, C08007.

Su, N., Liu, F., & Anh, V. (2003). Tides as phase-modulated waves inducing periodic groundwater flow in coastal aquifers overlaying a sloping impervious base. *Environmental Modelling & Software*, *18*, 937–942.

Swarzenski, P. W., Simonds, F. W., Paulson, A. J., Kruse, S., & Reich, C. (2007). Geochemical and geophysical examination of submarine groundwater discharge and associated nutrient loading estimates into lynch cove, Hood Canal, WA. *Environmental Science & Technology*, *41*, 7022–7029.

Szymczycha, B., Kroeger, K. D., & Pempkowiak, J. (2016). Significance of groundwater discharge along the coast of Poland as a source of dissolved metals to the southern Baltic Sea. *Marine Pollution Bulletin*, *109*, 151–162.

Taniguchi, M., Burnett, W., Cable, J., & Turner, J. (2003). Assessment methodologies of submarine groundwater discharge. *Land and Marine Hydrogeology*, *1*, 1–23.

Taniguchi, M., Dulai, H., Burnett, K. M., Santos, I. R., Sugimoto, R., Stieglitz, T., Kim, G., Moosdorf, N., & Burnett, W. C. (2019). Submarine groundwater discharge: Updates on its measurement techniques, geophysical drivers, magnitudes, and effects. *Frontiers in Environmental Science*, *7*, 141.

Taniguchi, M., Stieglitz, T., & Ishitobi, T. (2008). Temporal variability of water quality of submarine groundwater discharge in Ubatuba, Brazil. *Estuarine, Coastal and Shelf Science*, *76*, 484–492.

Terzaghi, K., Peck, R. B., & Mesri, G. (1996). *Soil mechanics in engineering practice*. John wiley & sons.

Thornley, J. D., Dutta, U., Douglas, J., & Yang, Z. J. (2021). Evaluation of horizontal to vertical spectral ratio and standard spectral ratio methods for mapping shear wave velocity across Anchorage, Alaska. *Soil Dynamics and Earthquake Engineering*, *150*, 106918.

Traiger, S. B., & Konar, B. (2017). Supply and survival: Glacial melt imposes limitations at the kelp microscopic life stage. *Botanica Marina*, *60*, 603–617.

Trefry, M., & Bekele, E. (2004). Structural characterization of an Island aquifer via tidal methods. *Water Resources Research*, *40*(1), W01505.

Varma, S., Turner, J., & Underschultz, J. (2010). Estimation of submarine groundwater discharge into Geographe Bay, Bunbury, western Australia. *Journal of Geochemical Exploration*, *106*, 197–210.

Viso, R., McCoy, C., Gayes, P., & Quafisi, D. (2010). Geological controls on submarine groundwater discharge in Long Bay, South Carolina (USA). *Continental Shelf Research*, *30*, 335–341.

Vuković, M. T., & Soro, A. (1992). Determination of hydraulic conductivity of porous media from grain-size composition.

Weitzman, B., Konar, B., Iken, K., Coletti, H., Monson, D., Suryan, R., Dean, T., Hondolero, D., & Lindeberg, M. (2021). Changes in rocky intertidal community structure during a marine heatwave in the northern Gulf of Alaska. *Frontiers in Marine Science*, *8*, 556820.

Whitney, E. J., Beaudreau, A. H., & Howe, E. R. (2018). Using stable isotopes to assess the contribution of terrestrial and riverine organic matter to diets of nearshore marine consumers in a glacially influenced estuary. *Estuaries and Coasts*, *41*, 193–205.

Wiles, G. C. (1992). *Holocene glacial fluctuations in the southern Kenai Mountains*. State University of New York at Buffalo.

Wiles, G. C., & Calkin, P. E. (1994). Late Holocene, high-resolution glacial chronologies and climate, Kenai Mountains, Alaska. *Geological Society of America Bulletin*, *106*, 281–303.

Winnick, M. J., Carroll, R. W., Williams, K. H., Maxwell, R. M., Dong, W., & Maher, K. (2017). Snowmelt controls on concentration-discharge relationships and the balance of oxidative and acid-base weathering fluxes in an alpine catchment, East River, Colorado. *Water Resources Research*, *53*, 2507–2523.

Wunsch, C., & Stammer, D. (1997). Atmospheric loading and the oceanic "inverted barometer" effect. *Reviews of Geophysics*, *35*, 79–107.

Young, J. C., Pettit, E., Arendt, A., Hood, E., Liston, G. E., & Beamer, J. (2021). A changing hydrological regime: Trends in magnitude and timing of glacier ice melt and glacier runoff in a high latitude coastal watershed. *Water Resources Research*, *57*, e2020WR027404.

Zemp, M., Huss, M., Thibert, E., Eckert, N., McNabb, R., Huber, J., Barandun, M., Machguth, H., Nussbaumer, S. U., Gärtner-Roer, I., Thomson, L., Paul, F., Maussion, F., Kutuzov, S., & Cogley, J. G. (2019). Global glacier mass changes and their contributions to sea-level rise from 1961 to 2016. *Nature*, *568*, 382–386. https://doi.org/10.1038/s41586-019-1071-0

Zhang, M., Hao, Y., Zhao, Z., Wang, T., & Yang, L. (2021). Estimation of coastal aquifer properties: A review of the tidal method based on theoretical solutions. *Wiley interdisciplinary reviews Water*, *8*, e1498.

Zhou, Y., Sawyer, A. H., David, C. H., & Famiglietti, J. S. (2019). Fresh submarine groundwater discharge to the near-global coast. *Geophysical Research Letters*, *46*, 5855–5863.

SUPPORTING INFORMATION

Additional supporting information can be found online in the Supporting Information section at the end of this article.

How to cite this article: Russo, A. A., Jenckes, J., Boutt, D. F., Munk, J., Kirshen, A., & Munk, L. A. (2024). Physical and chemical characterization of remote coastal aquifers and submarine groundwater discharge from a glacierized watershed. *Hydrological Processes*, *38*(7), e15240. https://doi.org/10.1002/hyp.15240